

# Devices for spin injection & detection in graphite

Master's thesis of B. Zijlstra

Submitted September 13<sup>th</sup>, 2011

## Supervisors:

Dr. ir. Michel de Jong  
Dr. Johnny Wong

## Tutoring committee:

Prof. dr. ir. Wilfred van der Wiel<sup>†</sup>  
Prof. dr. ir. Harold Zandvliet<sup>‡</sup>  
Dr. ir. Michel de Jong<sup>†</sup>  
Dr. Johnny Wong<sup>†</sup>

<sup>†</sup>NanoElectronics (NE) group, EEMCS faculty, University of Twente

<sup>‡</sup>Physics of Interfaces and Nanomaterials (PIN) group, TNW faculty, University of Twente

NANO ELECTRONICS.

**MESA+**  
INSTITUTE FOR NANOTECHNOLOGY

**UNIVERSITY OF TWENTE.**



## Abstract

Graphene is an interesting material for applications in organic spintronics, because of its high mobility and its predicted long spin relaxation times. In practice however, only spin relaxation lengths up to 1-2  $\mu\text{m}$  have been observed [1]. Materials in close proximity to graphene have been suspected to significantly influence its spintronic properties. In thick stacks of graphene monolayers, aka graphite, the transport of spins would be less affected by such interface effects. The ultimate goal of this master thesis was to measure the spin relaxation length and/or time in bulk graphite. Therefore, a fabrication procedure had to be developed to make devices on graphite substrates that would allow for this type of probing.

Using shadow mask deposition, devices with a vertical spin valve geometry were fabricated. However, this device geometry is not suitable for non-local probing, and electrical measurements indicated bad performance. Simultaneously, a fabrication procedure was developed, in which a combination of e-beam lithography and photolithography was used to fabricate devices with a lateral geometry. Despite of the initial problems in fabricating these devices, most difficulties in the fabrication procedure were resolved and lateral devices could, eventually, be made readily.

Electrical measurements showed that these devices still often showed undesired and unpredictable behavior. The problems were presumed to be caused by defective tunnel barriers. In the final stages of this project, some electrodes were made that showed good tunneling behavior, but the fabrication modifications that had led to this improvement, had also caused the electrodes to become mechanically unstable at the low temperatures that were required for spin dependent transport measurements. Subsequent Hanle measurements with these defective tunnel barriers did not show any Hanle peaks, but instead a (spurious) LMR effect was observed.



## Table of Contents

Abstract .....	3
Chapter 1: Motivation .....	6
Chapter 2: Physical background .....	7
2.1 Spintronics .....	7
2.2 Applications .....	10
2.3 Organic spintronics .....	13
2.4 Spin injection and detection .....	17
Chapter 3: Device fabrication .....	20
3.1 Device lay-outs .....	20
Lateral devices .....	21
Vertical devices .....	23
3.2 Substrate preparation .....	24
3.3 Contact patterning .....	25
Photolithography .....	25
E-beam lithography .....	27
Shadow mask deposition .....	28
3.4 Deposition and lift-off .....	29
Silicon Dioxide .....	30
Ferromagnetic stack .....	32
Contact pads .....	37
3.5 Wire bonding .....	37
Chapter 4: Experiments .....	40
4.1 Experimental methods .....	40
4.2 Tunnel barrier inspection .....	41
4.3 MR and Hanle measurements .....	48
Chapter 5: Conclusions and recommendations .....	51
References .....	52
Appendix A: Procedures and recipes .....	54
Appendix B: Mask designs .....	58

## Chapter 1: Motivation

Spintronics is a relatively novel branch of electronics that seeks to include the spin of electrons as an additional functional parameter in electronic devices. Spintronics gained a major boost in 1988, when, in thin-film structures of alternating ferromagnetic and non-magnetic materials, a giant magnetoresistance (GMR) was observed.

GMR and the later developed tunnel magnetoresistance (TMR) structures have since found applications ranging from magnetic hard disk drive read heads to magnetoresistive random access memory (MRAM). However, spintronics has not yet penetrated into the domain of computational devices, though it offers exciting new possibilities. Incorporation of ferromagnetic materials into semiconductor device structures, could for example lead to a combination of electronic switching and magnetic memory functionalities in a single device. Moreover, hybrid structures of spintronic and traditional electronic elements are expected to hold significant advantages; like non-volatility, increased processing speed, improved power efficiency and higher integration densities, over their traditional counterparts [2].

Most designs for three-terminal spintronic devices use one non-magnetic conducting material in which polarized electrons are injected. Polarized electrons in this region are supposed to keep their original spin information, unless they are influenced by some external, deliberately applied force. However, spins have a tendency to randomize over time in non-magnetic materials. The characteristic length over which the spins randomize, differs starkly between different materials and partly determines the achievable accumulation of injected spins. Since the performance of spintronic devices generally increases with a higher accumulation, there is a strong push in the spintronic community to look for materials with large spin relaxation lengths.

Inorganic semiconductors have high mobilities and low spin relaxation times, resulting in reasonable spin relaxation lengths. Organic semiconductors have, due to their composition, potentially high spin relaxation times, but mostly suffer from low mobilities [3]. However, organic chemistry is known for its diversity in organic structures. Possibly, some organic materials could have just the right structure to combine relatively high mobilities with high spin relaxation times, thus yielding very long spin relaxation lengths.

Graphene, a recently discovered 2D sheet of carbon atoms in a hexagonal lattice, is a potential candidate. Since it consists almost entirely out of  $^{12}\text{C}$ , both hyperfine interactions and spin-orbit coupling are supposed to be very small (even compared to other organic materials), which should result in very high spin relaxation times. Its mobility is also very high compared to other organic materials; values in excess of  $10000 \text{ cm}^2(\text{Vs})^{-1}$  have been observed at room temperature [4].

However, measured spin relaxation lengths of graphene proved to be disappointing [1]. This can be especially attributed to spin relaxation time, which was small for an organic material. One possible cause for the low spin relaxation time could lie in the fact that graphene is only one layer thick and thus its spintronic properties could be significantly influenced by nearby materials. Since this is an interface effect; its influence should be lesser in a thick stack of graphene layers (graphite). In this research project we will build electronic devices to measure the spin relaxation time and length in thick graphite and attempt to indeed measure them. A high spin relaxation time in graphite could validate this notion and could possibly lead to a search for more appropriate material combinations for graphene.

## Chapter 2: Physical background

During the late 1980's a novel branch of electronics arose: spin electronics, also abbreviated as spintronics. In spintronics both the charge and spin of electrons are used to design novel electronic functionalities. Since this field of research is relatively new and because the wider community is unfamiliar with its (potential) applications, this chapter will seek to briefly introduce its principles and related concepts relevant to this thesis.

### 2.1 Spintronics

Magnetic fields derive from two distinct sources: movement of charges and the intrinsic angular momentum of individual elementary particles, also called spin. The spin of an electron is of quantum mechanical origin and is quantized, either taking the value  $+\frac{1}{2}$  (up) or  $-\frac{1}{2}$  (down). Because of its spin, each electron has a tiny magnetic moment, though this does not directly translate into materials having a net magnetic moment. In elements with an even number of electrons, the electrons of an atom are usually divided equally between the two different species. In elements with an odd number of electrons, the electron with an unpaired spin can pair up with an unpaired spin of a neighboring atom, again leading to zero net-spin.

However in a few materials the electrons with unpaired spin do not pair up, but instead all unpaired spins line up parallel with each other: a ferromagnet. Two relevant forces are at play in causing ferromagnetic behavior: magnetic dipole-dipole interaction and exchange interaction. Dipole-dipole magnetic interaction is the force that reduces stray magnetic fields by ordering bulk magnets in an anti-parallel fashion. Exchange interaction instead seeks to minimize the electrostatic repulsion between neighboring electrons. The electrostatic repulsion of neighboring electrons with unpaired spin and overlapping orbitals can, under certain conditions, be minimized by parallelizing their spins. In the case of ferromagnets, this is indeed the case. However exchange interaction is a short-range quantum mechanical phenomenon, and thus the dipole-dipole magnetic interaction becomes dominant again at larger length scales. Bulk ferromagnets are therefore divided into domains of differing magnetization to reduce the stray field. These domains are separated by domain walls; a region in which there is a shifting gradient of spin direction. An additional player in ferromagnetic behavior is the thermal energy, which tends to randomize the spin polarization of a ferromagnet. Above the Curie temperature ( $T_c$ ) ferromagnetism disappears entirely; the exact Curie temperature of a certain ferromagnet depends mainly on the strength of the exchange interaction.

A current in a ferromagnetic material is also polarized: there is a numerical difference between the two spin-species in the electrons that are carrying the current. Ferromagnetic materials have long been known to have anomalous resistance behavior compared to ordinary conductors, which was explained by Mott in 1936 to be a result of this polarization [5]. Below a certain temperature, the occurrence of spin-flip scattering, a process of a spin changing its orientation, is much lower than its non-flip scattering rate [2]. Under these conditions spin-flip scattering can be neglected and the two spin species could be regarded as two separate conducting channels. This "two-channel" model can be seen as the basis of what is nowadays called spintronics and is still used today.

A major development in the field of spintronics was the discovery of giant magnetoresistance (GMR) [6]. This effect was more than two orders of magnitude larger than the previously observed

anisotropic magnetoresistance (AMR) and Lorentz magnetoresistance (LMR). It was observed in 1988 in a stack of Fe/Cr/Fe [5]. In figure 2.1.1, a schematic diagram of a GMR resistance curve can be seen.

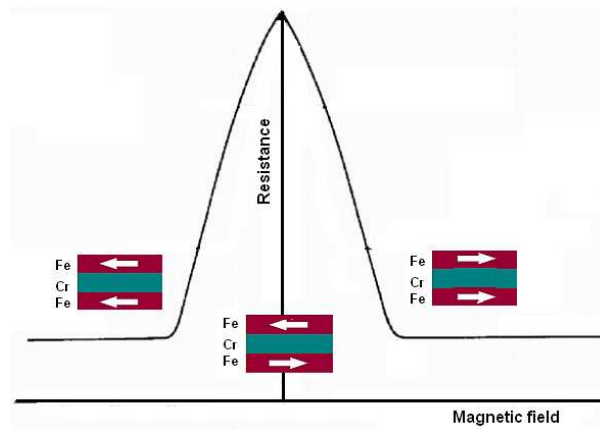


**Fig. 2.1.1:** Schematic illustration of the GMR effect and its resistance curve.

For obtaining GMR, a stack of a ferromagnet (FM), a non-magnetic metal (NM) and again a ferromagnet is used. The ferromagnetic layers should have different magnetic coercivities, so that they can be switched independently. Under a sweeping external magnetic field one FM layer switches first, leading to an anti parallel (AP) configuration; later the second FM layer switches also, resulting again in a parallel (P), switched configuration. The NM layer serves both as a conductor and as a separation medium to change the coupling between the ferromagnetic layers [2]. In the current perpendicular to plane geometry (CPP), a polarized current is injected from the first FM into the NM, travels through the NM and gets injected into the second FM. The giant resistance change is mainly generated near the two interfaces (FM/NM and NM/FM). The mobility of minority spin carriers gets reduced close to these interfaces by scattering events, while majority carriers can travel comparatively unscathed [2]. For an anti parallel configuration both up and down electrons can be considered a minority spin at one of the two interfaces. Thus both channels of spin species are blocked, which translates into a high resistance. However in a parallel configuration one of the spin species can travel efficiently, leading to a low total resistance. Since its discovery, GMR has found application in the read-heads for detecting magnetic fields with high spatial precision and has yielded its discoverers (Fert and Grünberg) a Nobel Prize.

However, the GMR effect is not necessarily the most effective way to generate high resistance differences under influence of an external magnetic field [2] and only a limited number of material combinations are possible. Unlike what was suggested in the previous paragraph, GMR does not utilize two separate channels, but usually four. In figure 2.1.2 a schematic density of states (DOS) diagram for a ferromagnet is shown. The electrons near the Fermi energy, which carry most of the current, can in most FM materials have both an s- and d-character. The s-electrons are hardly polarized, but they have low effective masses compared to d-electrons and thus are responsible for most of the conduction. The d-electrons are more polarized due to the exchange interaction. However, again because of the exchange interaction, the d-band presents a spin-dependent density of states at the Fermi energy into which s-electrons can easily scatter. As a consequence minority s-electrons are more scattered into minority d-states (with high partial DOS at  $E_F$ ), reducing their mobility, while majority s-electrons experience less scattering into the majority d-states (with low partial DOS). This "bulk" GMR effect usually works conjunction with the interface GMR effect.

However, they act in some cases in opposition to each other, effectively reducing the overall GMR effect.

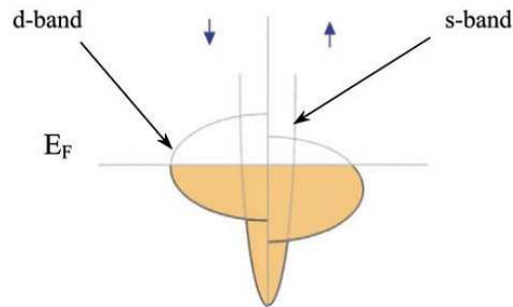


**Fig. 2.1.2:** Schematic for partial DOS of a ferromagnet for minority spins (left) and majority electrons (right) [2]

A way to overcome the problem originating from competing mobility asymmetries associated with GMR devices, is to eliminate the conducting medium altogether. By replacing the conducting material in between the two ferromagnets with an insulator (also called tunnel barrier), current can only be transmitted by quantum mechanical tunneling. The resistance effect generated by these kinds of stacks is called tunnel magnetoresistance (TMR). The operating principle of a magnetic tunnel junction (MTJ) is schematically shown in figure 2.1.3.

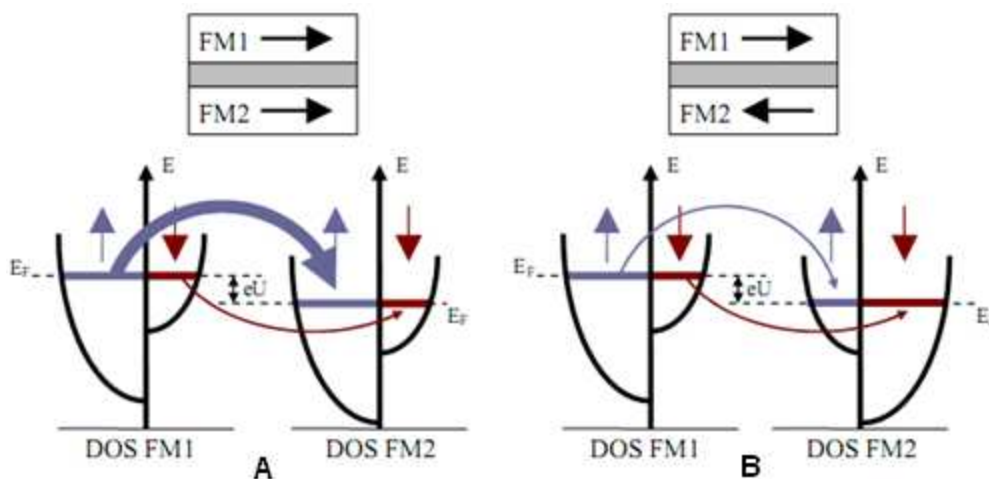


**Fig. 2.1.3:** Schematic of the densities of states for a biased MTJ in (a) a parallel and (b) anti-parallel configuration [5].

Since spin orientation is conserved during tunneling, an electron can only tunnel from a given spin subband in the first FM electrode into the same subband in the second FM electrode. The tunneling rate for a certain spin species at a particular energy is proportional to the product of the two densities of states at that energy at each side of the tunneling barrier [2]. In the case of a TMR device in a parallel configuration, this leads to a high tunneling rate for the majority spin and thus a low total resistance. In the anti parallel configuration both spin species get a low tunneling rate and thus the TMR device shows a high total resistance.

A compact equation for the TMR effect was derived by Jullière, assuming energy and spin conservation during tunneling. Although this equation has already been modified nowadays to conform to experimental observations, it still gives a good basic insight [4].

$$TMR = \frac{R_{AP} - R_P}{R_P} = \frac{2P_1P_2}{1 - P_1P_2} \quad (1)$$

Where  $R_{A(P)}$  is the resistance in the anti- and parallel configuration,  $N_i(E_F)$  the DOS at the Fermi energy with that spin-state and  $P_{1(2)}$  the polarization of the first (second) FM electrode with:

$$P_i = \frac{N_{i\uparrow}(E_F) - N_{i\downarrow}(E_F)}{N_{i\uparrow}(E_F) + N_{i\downarrow}(E_F)} \quad (2)$$

## 2.2 Applications

Since their discovery both the GMR and the TMR effect have been applied in read heads of hard disks to detect changes in magnetic fields with high spatial precision. However the tool-kit of spintronics is expected to yield more interesting electronic functionalities. Since molecular spintronics is still in its infancy, we will focus solely on future applications of “bulk” spintronics.

There are a number of building blocks in spintronics. The starting point in a spintronic device is usually generating a polarized current. This is commonly done by using ordinary ferromagnetic materials, like for example Co, Fe and permalloy. As can be seen in equation 1, the performance of a TMR spin valve, and by extension all spintronic devices, is best when having a completely polarized current. This is not the case for ordinary ferromagnetic materials, but there are some alternatives that can achieve an almost completely polarized current. In half-metallic ferromagnets (HMF) the electronic band structure is split by exchange interaction in such a way that only one spin channel has available states at the Fermi surface, resulting, in theory, in a current of only one spin species. Often a mixed oxide of lanthanum strontium manganite (LSMO) is used, but  $CrO_2$  and some Heusler alloys also exhibit this property [2]. However in practice these materials do not achieve this due to interface problems. A different approach is used in something called a spin-filter. Electrons tunnel through a magnetic tunnel barrier from a NM to another NM. Since the tunnel barrier is magnetic, the two spin species experience different barrier heights, resulting in different tunneling rates. The tunneling rates decrease exponentially both with the barrier height and with the thickness, so the polarization can be tuned to be very high [2]. However, the materials commonly used for these barriers (Eu-chalcogenides) have low  $T_c$ 's and thus no spin filtering has been observed at room temperature (RT) [7]. Materials with such high polarizations are however potentially attractive for future applications in quantum computing.

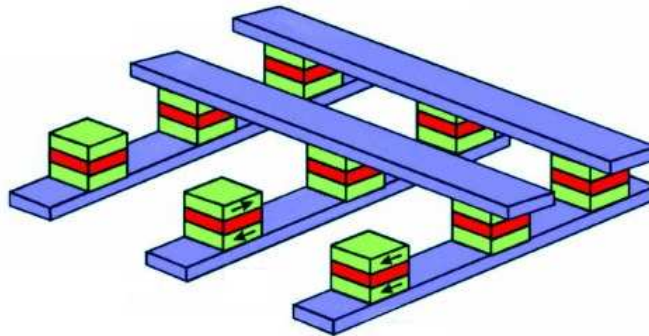


**Fig. 2.2.1:** Schematic illustration of an MRAM cell.

A relatively recent application of spintronics is in a non-volatile computer memory element, called magnetoresistive random access memory (MRAM). MRAM consists out of an array of MTJ's, as shown in figure 2.2.1. One of the ferromagnetic layers is often pinned by sandwiching it with an anti-ferromagnetic layer. Each MTJ is contacted by two wires and a transistor, the contact being switched on by the transistor. The two magnetic states of the MTJ, the parallel and anti parallel configuration, give different resistances and thus correspond to the two memory states. The memory can be rewritten by a magnetic field generated by the currents through the two wires. However this way of switching limits the memory density compared to competing memory types, since at high densities a neighboring MTJ can also be accidentally switched. Some ways to resolve this are currently under development. One approach is to heat one MTJ up, thus allowing it to switch at a lower magnetic field, and afterward cooling it down again. Another approach would be to transfer angular momentum from an additional magnetic layer, by injecting a polarized current from it into the thin ferromagnetic electrode in order to switch its magnetization; a process called spin transfer torque (STT) switching. Though this has recently been demonstrated to work [5], the amount of current needed to switch is currently too high to make it commercially viable [8]. Pseudo-switching by moving magnetic domain walls might also be possible, but is still in its infancy [2]. A more exotic solution could come from dilute magnetic semiconductors (DMS). These materials act as semiconductors, but also display a form of ferromagnetism mediated by charge carrier density and can offer quite high polarizations [9]. However known DMS materials have  $T_c$ 's below room temperature and research into potential materials having high  $T_c$ 's is fraught with controversy, making a room temperature DMS, at least for the near future, a mythical holy grail in spintronics.

Both the TMR based magnetic read heads and MRAM are examples of two-terminal devices. To make a lasting impact into the computing industry, spintronics should move into the field of three terminal devices. In terms of energy consumption and switching speeds, spintronic devices have been suggested to hold a significant advantage compared to their electronic counterparts [2]; something that would be welcome to an industry that is rapidly approaching the physical limits of Moore's law.

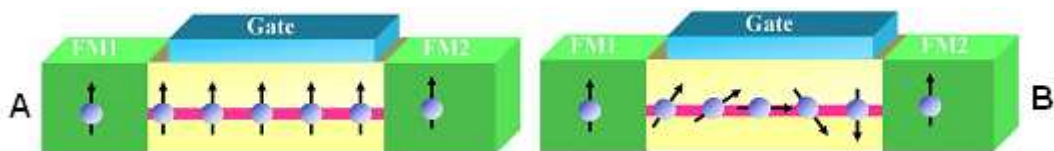


**Fig. 2.2.2:** Schematic illustration of a Datta-Das transistor (a) in the ON state and (b) in the OFF state [8].

In figure 2.2.2 a schematic illustration of a Datta-Das transistor (or spinFET) is shown. Though there are many three terminal device configurations possible, the spinFET concept is among the most well known. In a spinFET polarized electrons are injected from a ferromagnetic source into a non-magnetic conducting material. Under influence of a source-collector potential a current, including some of the injected electrons, runs from the source to the collector. At the collector local electrons are injected from the non-magnetic material into the ferromagnetic collector again. To electrons travelling through the spinFET channel at near-relativistic speeds, the electric field originating from the gate appears partially magnetic, thus causing precession of their spins (Rashba effect) [8]. In a parallel configuration of the magnetic source and collector, at a certain gate bias the electrons execute an integral number  $N$  of spin precessions. As a consequence they arrive at the collector with the same spin as the majority spin of the collector, resulting in high device conductance. However, a slightly different gate voltage can result in  $N + \frac{1}{2}$  precessions, thus arriving at the collector with

minority spin type, resulting in a low device conductance. The resulting device behaves similar to a normal FET, with the additional feature of its electrodes being sensitive to an external magnetic field.

However, because of practical difficulties, a working spinFET device has not yet been realized. For starters, efficiently injecting a polarized current from a ferromagnet (HMFs excluded) into a semiconductor via an Ohmic contact turned out to be problematic [2]. Due to interface effects and the difference in DOS between metallic ferromagnets and semiconductors spins easily flip near the interface, consequently reducing the accumulation in the semiconductor. Aside from this spin injection problem, there is a big difference in conductivity between ferromagnets and semiconductors. Because of this conductivity mismatch, the difference in resistance between the different magnetic configurations gets dwarfed by the total resistance of the semiconductor; potentially masking it. Therefore, an intermediate layer with a large spin dependent resistance is often sandwiched in between a ferromagnet and a semiconductor. Non-magnetic tunnel barriers are often used for this purpose, though magnetic tunnel barriers and Schottky barriers are also usable under some circumstances [2].

A more serious obstacle for three terminal devices comes from spin relaxation. In a non-magnetic material, injected excess spins have a tendency to randomize over time via a number of different mechanisms [5]. On the length scales (nm) of GMR devices, spin relaxation in the NM could be neglected. However, for the length scales required for three terminal devices, spin relaxation does become very significant. In a semiconductor channel, excess spin density at distance  $x$  is approximately given by [2]:

$$n = n_0 e^{-x/l_s} \quad (3)$$

In which  $n_0$  is the excess spin density at the injection site and  $l_s$  is the spin relaxation length. The spin relaxation length is in turn given by:

$$l_s = \sqrt{\tau D} \quad (4)$$

In which  $\tau$ , is the spin relaxation time.  $D$  is the diffusion coefficient and scales linearly with the electronic mobility. The excess spin density at the injection site can also be written as:

$$n_0 = \frac{P_s J}{q} \sqrt{\frac{\tau}{D}} \quad (5)$$

In which  $P_s$  is the polarization at Fermi energy of the injecting ferromagnetic source,  $J$  the current density and  $q$  the carrier's charge. The crucial focus for a three terminal device lies in getting a high excess spin density close to the collector, from which polarized electrons can be injected to yield a TMR signal. In order to achieve this, solutions have to be found to get materials with high polarizations (discussed previously) and high spin relaxation lengths. As can be seen in equation 4, spin relaxation lengths are determined by the spin relaxation time and mobility in a material. Reasonable spin diffusion lengths have been measured in inorganic semiconductors. For example in silicon, a spin diffusion length larger than 230 nm at room temperature was recently observed [10]. Though these materials do have relatively high mobilities, they suffer from low spin relaxation times.

## 2.3 Organic spintronics

Organic materials in contrast can have high spin relaxation times, but generally display low mobilities [3]. For a long time organic materials were therefore only used as insulators, but nowadays many organic conductors have been found and have been implemented in a number of successful applications. Among the potential advantages of organic conductors are: the possibility of chemical tuning of electronic functionality, easy structural modification, the possibility of self-assembly and mechanical flexibility [4]. These advantages could allow the fabrication of low-weight, large area and low-cost electronic devices. Organic spintronics seeks to integrate organic materials, and their advantages, into traditional spintronics. Although in terms of mobilities, organic materials are currently inferior to inorganic semiconductors; this is still a developing field. With an improving balance between spin relaxation times and mobility, organic spintronics could some day rival or surpass its inorganic counterpart.

Electronic transport in an organic material is often different from transport in inorganic materials. Generally two different charge transport mechanism can be distinguished: hopping and band-transport. In disordered organic materials, transport occurs by carriers hopping from one localized molecular state to the next. This type of transport is highly influenced by temperature and carrier mobilities are low. Organic materials that show good mobilities are almost all  $\pi$ -conjugated materials [4]. Electrons in a  $\pi$ -bond are delocalized along the molecule, thus allowing for easy transport along the molecule. If these molecules are ordered in the correct way, they could potentially display band-like transport at low temperatures and would thus display high mobilities. Organic single crystals (OSC) of for example rubrene are therefore a hot research topic and mobilities of up to  $40 \text{ cm}^2(\text{Vs})^{-1}$  at room temperature have been reported [11]. Another detrimental factor to mobilities in organic materials comes from polaron formation [4]. Bonding forces in an organic material are comparatively low. Therefore, while passing through an organic material, a charge carrier experiences a kind of drag, because it deforms its surroundings. The charge carrier and the deformation together are called a polaron, a quasi-particle.

Spin relaxation in a material occurs via a number of different mechanisms that rely on spin-orbit coupling and hyperfine interactions to flip the spin [5]. Spin-orbit coupling generally increases with atomic number  $Z$  and is commonly assumed to scale roughly with  $Z^4$  [4]. The main atomic constituents of organic conductors (C, H and N) have low  $Z$ -values, which would thus result in relatively low spin-orbit coupling. Hyperfine interactions originate from the coupling between an electron's spin and nuclear spins in a material [4]. The main constituents of an organic semiconductor are carbon atoms, which in turn are made up for roughly 99% out of  $^{12}\text{C}$ ; an isotope having zero nuclear spin. Though an organic material does contain nuclear magnetic dipole moments (from  $^{13}\text{C}$ ,  $^1\text{H}$  and  $^{14}\text{N}$ ), hyperfine interactions are thought to be comparatively small [4].

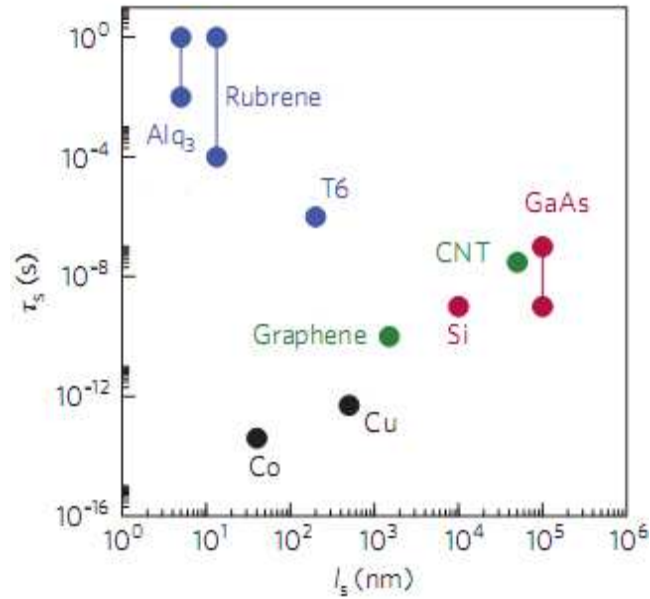


**Fig. 2.3.1:** Spin relaxation  $l_s$  vs. spin relaxation time  $\tau_s$  for various materials [12].

In figure 2.3.1 observed spin relaxation times and lengths for various materials are shown. It should be noted that this graph only allows for rough comparisons, since experimental settings and measurement techniques differ for different presented values. Two of these materials are of particular interest to this thesis: (multi walled) carbon nanotubes (CNT) and graphene. Graphene is a two-dimensional sheet of carbon atoms in a hexagonal lattice. Graphene is a very interesting material, both for electronic and spintronic applications [4]. It is a zero-gap semiconductor with a conical (Dirac) energy dispersion near its Fermi energy, resulting in charge carriers behaving like mass-less particles. Transport in graphene is ballistic; charge carriers can travel large distances without scattering and very high mobilities ( $>10000 \text{ cm}^2(\text{Vs})^{-1}$ ) have been observed at room temperature [4]. Moreover, due to its low scattering rate and mass-less particles, many of its unique quantum effects can survive even at room temperature. Due to its high mobility, good conductance of holes and electrons, expected low spin-orbit coupling (low Z) and low hyperfine interactions (only  $^{13}\text{C}$ ), graphene is expected to have high spin relaxation times and lengths, making it an excellent material for transporting spins. In addition, the earlier mentioned spinFET concept functions best in the case of a 2D electron gas (2DEG), making graphene, one of the few currently available 2D materials, very attractive.

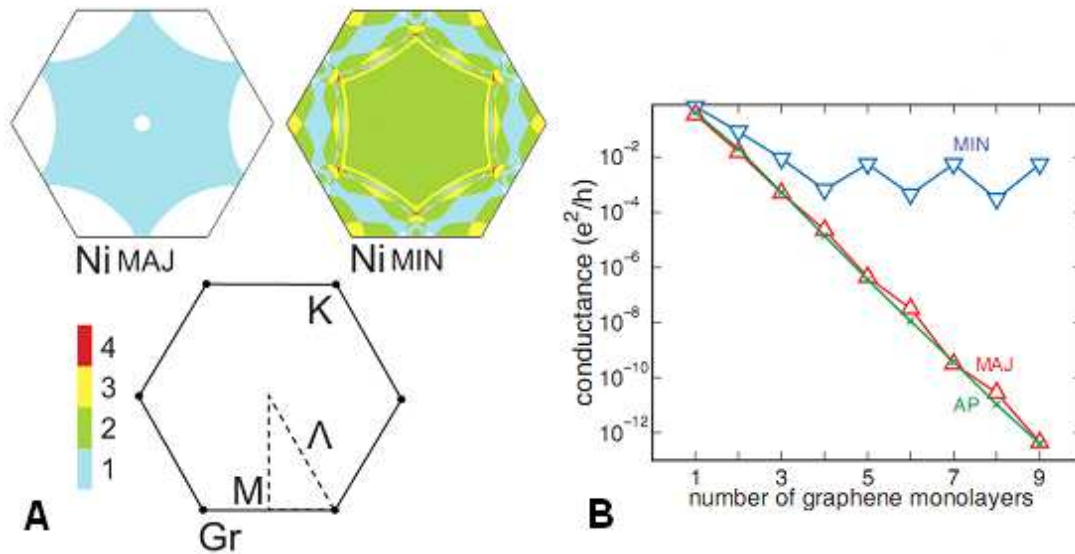


**Fig. 2.3.2:** (a) Fermi surface projections for fcc Ni (111) majority and minority spins and graphene/graphite. (b) Conductance for Ni/Gr<sub>n</sub>/Ni stack as a function of the number of graphene monolayers for minority spin in P (blue), majority spin in P (red) and both carriers in AP (green) [13].

However, there are more reasons that warrant spintronic research of graphene [14], [15]. Currently, very high TMR values have been observed in epitaxial stacks of Fe/MgO/Fe (180% at RT) [13]. Epitaxial growth is difficult to achieve, partly because there is a relatively large lattice mismatch of 3.8 % between Fe and MgO. Therefore alloys of FeCoB instead of Fe, are sometimes used, which, after a post annealing treatment, form a more or less epitaxial structure with MgO [16]. However, TMR values (and spin injection) in these systems remain very sensitive to the exact interface structure and there is a significant gap between observed and predicted TMR values.

Recently, Kelly et al. proposed a CPP MTJ of Ni/graphene/Ni or Co/graphene/Co that would be less sensitive to interface structure and would function in a manner akin to the earlier mentioned spin-filter [13]. The functioning principle of these MTJs can be seen in figure 2.3.2a. At the Fermi energy, graphene only has states at the K-point (or Dirac point). Ni majority electrons do not have available states at or close to the K-point, but Ni minority electrons do. As a consequence, in case of conservation of crystal momentum, majority electrons can only tunnel through the graphene separation layer, while minority electrons can both tunnel and use the graphene channel at the K-state. The rate of tunneling decreases exponentially with the number of graphene monolayers, while the transport of minority electrons through the channel at the K-state remains relatively constant, as can be seen in figure 2.3.2b. For conservation of momentum, an epitaxial interface between graphene and the FM is needed. The lattice mismatch between Ni/graphene and Co/graphene is only 1.3% and 1.9%, respectively. To prevent hybridization between the FM and graphene, a small amount of Cu is needed at the interface [13]. Density functional theory (DFT) calculations of Kelly et al. suggest that, even for a rough interface with a 50% mix of Cu and Ni, the TMR will not be lower than 230% [14]. However, in practice the proposed interface has not been yet realized. Both Ni and Co display island growth on graphene [17], [18], and growing more than one monolayer of graphene uniformly on these materials is very hard. A possibility for epitaxial growth could however come from a similar approach as post annealing FeCoB.

A CNT is basically a sheet of graphene, which is folded into a cylindrical shape of a few nanometers in diameter; the electronic structure depending on the exact folding (metallic or semiconductor) [4]. When returning again to graph 2.3.1, it can be seen that, with regard to the spin relaxation length, the performance of a CNT is almost on par with GaAs. However graphene, with a spin relaxation length between 1.5 and 2  $\mu\text{m}$  [1], [19], lags orders of magnitude behind. It begs the question why there is such a big gap between graphene and a CNT, though they share high mobilities and have the same atomic building blocks.

Aside from the fact that the structure, and thus the electronic behavior, is different, there are also additional explanations possible. One of these was already hinted at: the measurement settings are not comparable. The CNT measurement involves a single molecule [20], while the graphene measurement comes from a large flake. Another cause could originate from a difference in history. Graphene was discovered in 2004 [21]; while carbon nanotubes have been known at least since 1991. Graphene was first made by mechanical exfoliation, though since then, many other fabrication techniques have reported [22], [23]. The graphene in figure 2.3.1, was made by exfoliation and displays a mobility of  $2000 \text{ cm}^2 (\text{Vs})^{-1}$  [1]. Mechanical exfoliation is known to create more defects than some alternatives, which can serve as (spin) scattering sites. Tombros et al. concede in their paper, that by improving their fabrication procedures, both  $\tau$  and  $\mu$ , and thus  $l_s$ , could be increased.

A different detrimental factor could come from neighboring materials. Graphene is only one sheet of atoms thick (0.33 nm) and some nearby dielectrics and metals can significantly alter its electronic properties [4]. Since electronic properties can be modified; it is not inconceivable that this also applies to spintronic properties. Since this suspected influence of neighboring materials on graphene is only a (near-) interface effect, its influence should be far less noticeable on spin transport in bulk graphite; which consist out of Bernal stacked graphene sheets. If measurements indicate that graphite indeed has superior spin relaxation times, it would indicate that this notion could be valid.

## 2.4 Spin injection and detection

Detection of injected spins is not a trivial matter. There are number of different techniques, but detection by electronic measurements is commonly used and is applicable for most materials. A simple two terminal measurement of magnetoresistance (MR) would seem the most logical approach, but does not irrefutably prove spin injection. So called spurious effects give rise to MR effects, but are in fact not related to the earlier discussed GMR and TMR effects [4]. Among the many spurious effects is the earlier mentioned LMR effect. The Lorentz force curves the electron trajectories and is especially relevant in materials with relatively long mean free paths. The Lorentz magnetoresistance is of the order [4]:

$$(l_e/l_B)^4 \quad (6)$$

In which the magnetic length,  $l_B$ , can also be rewritten as:

$$l_B = \sqrt{\hbar/(eB)} \quad (7)$$

Where  $\hbar$  is Planck's constant and  $e$  is the elementary charge. Though two terminal measurements provide only circumstantial evidence for spin injection, some three or four terminal measurement schemes do provide direct evidence.

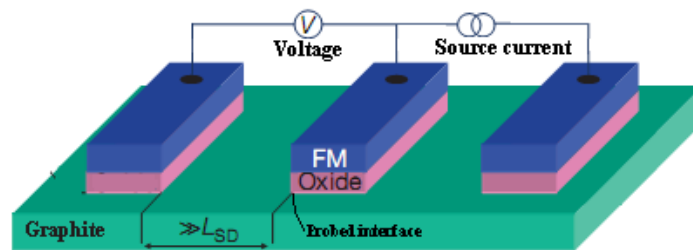


**Fig. 2.4.1:** Device geometry for a Hanle measurement. The contacts are designated, from left to right, as 1, 2 and 3.

One of these measurement schemes is based on the electrical Hanle effect. A device geometry of a Hanle measurement can be seen in figure 2.4.1. Electrons are injected from the electrode 2 into the graphite and a current runs from the electrode 2 to electrode 3. Excess spin electrons accumulate underneath electrode 2 and start to diffuse in the direction of electrode 1. Since the distance between electrode 2 and electrode 1 is far larger than the spin relaxation length, a negligible number of excess spin electrons arrive at electrode 1, because almost all of them randomize due to spin relaxation, beforehand. A voltage is now probed between electrode 1 and 2, instead of between the current carrying electrodes; a measurement configuration also known as “non-local” probing.

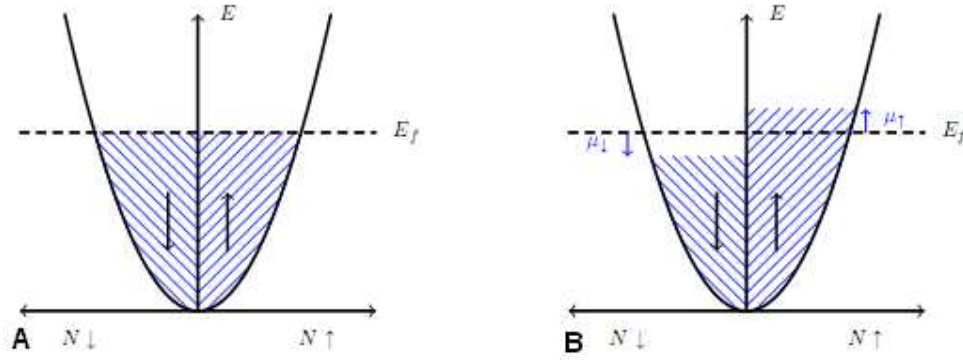


**Fig. 2.4.2:** Schematic diagram of the DOS of a non magnetic material (a) in equilibrium, and (b) with a finite spin accumulation [24].

In a material with a finite (injected) spin excess density both spin subbands do not have an equal occupation any more (figure 2.4.2b), but there is an imbalance. One of the spin subbands has gained  $\mu^\uparrow$  energy with respect to the Fermi level, while the other has lost  $\mu^\downarrow$ . This electrochemical potential is defined as  $\bar{\mu} = \mu + qV$ , where  $\mu$  is the chemical potential,  $q$  the charge of a charge carrier and  $V$  the voltage. The spin accumulation is defined as  $\Delta\mu = \mu^\uparrow - \mu^\downarrow$ , where  $\mu^{\uparrow\downarrow}$  is the electrochemical potential for each respective spin. There is a difference in spin accumulation between contact 1 and 2, which translates into a voltage difference between the contacts via [10]:

$$\Delta V = TSP \Delta\mu / 2 \quad (8)$$

In which TSP is the tunnel spin polarization of the ferromagnet-insulator interface.

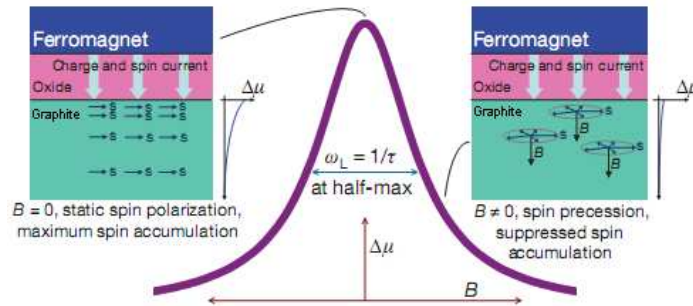


**Fig. 2.4.3:** Schematic illustration of a Hanle curve [10].

Applying a magnetic field perpendicular to carrier spins causes precession of the spins, which, via the (electrical) Hanle effect, reduces the spin accumulation underneath contact 2. This is picked up by the voltage probe, resulting in a curve similar to the one shown in figure 2.4.3. The spin precession frequency,  $\omega_L$  depends on the magnetic field,  $B$ , via [10]:

$$\omega_L = \frac{g\mu_B B}{\hbar} \quad (9)$$

Where  $g$  is the Landé  $g$ -factor,  $\mu_B$  is the Bohr magneton and  $\hbar$  is Planck's constant divided by  $2\pi$ . Since  $\omega_L = 1/\tau$  at half the maximum of the Hanle curve, the spin relaxation time can be directly extracted from a Hanle measurement. By doing a separate van der Pauw measurement to determine the mobility of graphite, the spin relaxation length can be estimated.

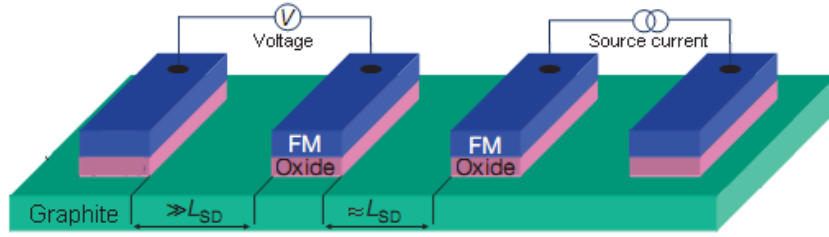


**Fig. 2.4.4:** Device geometry for a non-local measurement. The contacts are designated, from left to right, as 1, 2, 3 and 4.

In contrast, with the non-local measurement scheme the spin relaxation length can be directly measured. A device geometry of this measurement scheme can be seen in figure 2.4.4. Polarized electrons are injected from electrode 3 into graphite, accumulate and start diffusing towards electrode 2. Like in the Hanle geometry, external electrode 1 measures the potential difference with electrode 2. However, because the distance between 3 and 2 is close to the spin relaxation length, a finite spin accumulation develops at electrode 2. This gives rise to a voltage between contacts 2 and 1 in a similar manner as for the Hanle geometry. However, electrode 2 is also a ferromagnet-insulator stack and therefore responds differently to the different species. By sweeping the magnetic field parallel to the easy axes of the electrodes an AP and P configuration between electrode 2 and 3 can be achieved. The difference in non-local resistance between the two configurations is given by [25]:

$$R_{non-local} = \pm \frac{P^2 l_S}{2A\sigma} \exp(-L/l_S) \quad (10)$$

In which  $L$  is the spacing between electrodes 2 and 3,  $A$  their cross-sectional area and  $\sigma$  the electrical conductivity of graphite. By using equation 10 and measuring devices with differing  $L$ , the spin relaxation length can be extracted.

## Chapter 3: Device fabrication

This chapter describes the main activities of this work. A lot of effort was put in the development of fabrication procedures to make a working spintronic device on top of a HOPG substrate. Several techniques were used and a large number of samples were fabricated, which resulted in a number of partially working devices. This chapter is aiming to provide an insight into the device fabrication work that was performed and what kind of (resolved and unresolved) problems were encountered. Electrical measurements and other kinds of results are treated in the next chapter.

In this project the main three approaches in obtaining spin transport devices were optical lithography and e-beam lithography for fabricating lateral devices and shadow mask deposition for manufacturing vertical devices. Due to our choice for HOPG and its properties, we encountered a lot of problems that had no counterpart with regular silicon-substrates. The main problems with the structural fabrication were related to the patterning of resist layers on the substrate and the lift-off of deposited materials, so a large section of this chapter is devoted to those two problems.

### 3.1 Device lay-outs

In developing the fabrication process, several considerations had to be taken into account. Chief point among these considerations was the suspicion that the spin lifetimes in graphene/graphite mentioned in earlier publications, were being significantly influenced by the close proximity of an interface with non-graphite materials. In order to negate this suspected influence, only substrates with a thick graphite layer could be used. Since it is difficult to create a high-quality graphite layer of sufficient thickness on top of a substrate with existing fabrication methods, the choice was made to start with a substrate consisting entirely out of graphite.

The choice for a pure graphite substrate results, however, in a number of complications in the fabrication process. One of these is the fact is that graphite is not chemically robust, which makes most etching methods unsuitable, since the accumulated damage during the fabrication steps might degrade the quality of the graphite substrate. Because of this limitation only “soft” patterning processes based on lift-off processes or shadow mask deposition were used. The development of a fabrication process has been mostly focused on the former; in part because the resolution required for a non-local device geometry (see chapter 2.4), cannot be obtained by shadow mask deposition.

## Lateral devices

A schematic drawing of the lateral device lay-out can be seen in figure 3.1.1. The device design is based on a similar device that has been previously used in the NE-group to measure electrically created spin polarization in silicon [10]. It is designed to be used for both Hanle and non-local measurements (chapter 2.4), which requires at least four contacts to cancel spurious effects. There are two closely-spaced, narrow ferromagnetic contacts, which need to have different magnetic coercivities in order to perform non-local voltage measurements; something that is achieved by having different contact widths, resulting in different magnetic shape anisotropy. These two smaller contacts also need to be very close to each other, since otherwise spin signals would be difficult to measure due to the spin relaxation. The distances from the two big contacts to the smaller contacts are required to be far larger than the spin diffusion length, since they serve as reference/source contacts; their magnetic properties are not relevant.

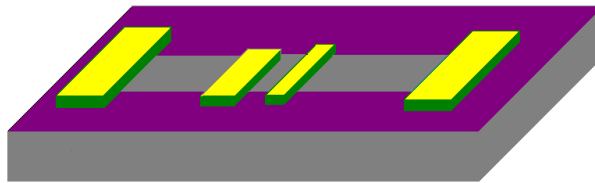


**Fig. 3.1.1:** Schematic drawing of a lateral device. Underlying is the graphite substrate (grey), which is partially isolated by the SiO<sub>2</sub> layer (purple). The magnetic contacts consist out of the Al<sub>2</sub>O<sub>3</sub> tunnel barrier and the ferromagnetic cobalt (together green), which is protected by the capping layer (yellow). The contacts are connected to a measurement apparatus via individual contact pads, which are not shown here.

The basic process flow for a lateral device can be seen in figure 3.1.2. First the graphite substrate is peeled with Scotch tape and put for a short while in an ultrasonication bath in order to make its surface flat and mechanically stable. The next step is to define a channel of 68 x 400 μm on the graphite using photolithography. On top of the developed photoresist a SiO<sub>2</sub> layer is deposited. The photoresist is subsequently removed in a lift-off operation with acetone, leaving a channel of uncovered graphite in the SiO<sub>2</sub>. The SiO<sub>2</sub> layer serves as an insulation layer for the later ferromagnetic contacts and the contact pads. The use of a channel instead of contact holes is the only significant difference with the earlier mentioned design [10]. Contact holes were a necessity in the earlier design, since ion beam etching was in that case used to pattern the later layers. However in the current design, spin transport through graphite is suspected to be degraded by interaction with materials in close proximity, thus requiring uncovered graphite/channels.

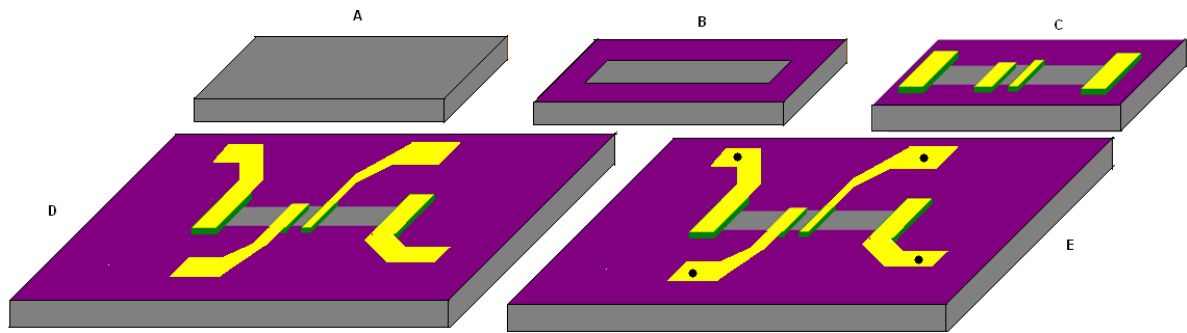


**Fig. 3.1.2:** Schematic diagram of the process flow for a lateral device in which graphite is colored grey, the tunnel barrier and ferromagnetic material green and the capping layers yellow. **(a)** HOPG substrate after peeling. **(b)** A  $\text{SiO}_2$  insulation layer is deposited with a channel of uncovered graphite remaining. **(c)** Ferromagnetic contacts are created. **(d)** Creation of contact pads. **(e)** The contact pads are connected to a sample holder via wire bonding with silver paste.

In a similar lift-off operation the ferromagnetic contacts are created. Instead of one material, this consists of a stack. The material at the bottom ( $\text{Al}_2\text{O}_3$ ) of the stack is directly in contact with the graphite and serves as a tunnel barrier. Tunnel barriers are used because of the conductivity mismatch problem (graphite-ferromagnet) and to increase the spin accumulation in the graphite. Since the graphite in the channels is not covered, plasma oxidation can not be used and so a 1-2 nm layer of  $\text{Al}_2\text{O}_3$  is deposited directly unto the graphite. In the middle of the stack there is the ferromagnetic material, cobalt, which provides the polarized electrons for injection. On top of this there is a capping layer, which prevents the oxidation of cobalt. For this capping layer different materials were used (Au and Al) and sometimes a combination of the two, in order to combat certain problems in the fabrication process (further discussed below).

The last lithography step is to define the contact pads (figure 3.1.2d). These contact pads connect the small, fragile ferromagnetic contacts to a larger contact, on which a wire can be bonded. The materials used for the contact pads differed. In the early stages a combination of Cr (adhesion layer) and Au was used, but in later samples Al, or a combination of Al and Au were also used. These contact pads were wire bonded with gold and aluminum wires.

## Vertical devices

The vertical devices were developed as a response to the problems with the lateral devices. Lift-off and the resolution of photolithography were problematic, which could be circumvented with the vertical geometry. However vertical devices were, because of their geometry, not suitable for non-local measurements, thus only two point and quasi-Hanle measurements were possible. When some of the problems with the lateral devices were solved, attempts with vertical devices were quickly abandoned due to the limitations in possible measurement schemes and the perceived persistent leakage of the tunnel barriers. A schematic drawing of a vertical device can be seen in figure 3.1.3. In the vertical geometry the contacts are defined by shadow mask deposition, which has a poor resolution. The contacts created are around an order of magnitude larger than their lateral counterparts (2.3x1 mm).

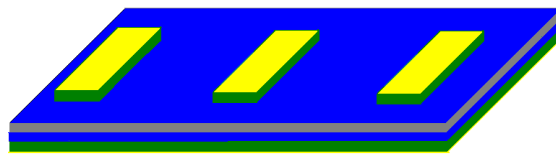


**Fig. 3.1.3:** Schematic drawing of a vertical device. There is a thin graphite layer in the middle (grey). On both sides of the graphite there is an Al<sub>2</sub>O<sub>3</sub> tunnel barrier (blue). The green, ferromagnetic layer consists in the lower case out of cobalt; in the upper case out of permalloy. On both sides there is an Al capping layer (yellow). The bottom side is attached to a Si substrate with double sided conducting carbon tape.

The fabrication of vertical devices starts again with a flattened graphite substrate and can be seen in figure 3.1.4. On top of the graphite an Al<sub>2</sub>O<sub>3</sub> tunnel barrier (1 nm) is deposited, followed by a ferromagnetic Co layer (50 nm) and an Au capping layer (3 nm). Subsequently double sided, conducting tape is applied to the deposition side of the graphite sample and all three deposited layers and some graphite layers are peeled off the graphite sample. The unused side of the double sided tape is attached to a Si substrate and once again inserted into the deposition chamber. On the backside of the peeled-off graphite an even (unpatterned) layer of Al<sub>2</sub>O<sub>3</sub> (1 nm) is deposited as a tunnel barrier. After this a layer of the ferromagnetic Permalloy (50 nm) is deposited through a shadow mask unto the tunnel barrier, thus defining the contacts. On top of the permalloy an Al capping layer (3 nm) is deposited. After that the contacts are connected by manual wire bonding.

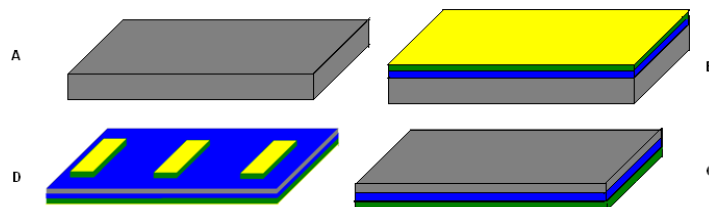


**Fig. 3.1.4:** Schematic diagram of the process flow for a lateral device in which graphite is colored grey, the tunnel barriers blue, ferromagnetic materials green, and the capping layers yellow. **(a)** HOPG substrate after ultrasonication. **(b)** Deposition of the ferromagnetic stack. **(c)** Ferromagnetic stack (including some graphite layers) is peeled off. **(d)** Ferromagnetic contacts are deposited by shadow mask deposition on the backside of the peeled off graphite.

## 3.2 Substrate preparation

Before discussing the actual fabrication process details, we would first like to elaborate on the properties of the bare graphite substrates themselves. Graphite is a natural polymorph of carbon and is known to be atomically flat on a small scale. The highest quality graphite substrates are single-crystals, but these substrates are expensive and small, which makes them unsuitable for use in a normal lithography process. Instead of these single crystals we use highly oriented pyrolytic graphite (HOPG), which should suffice for our purposes, since our devices have features in the micrometer regime.

A limited number of substrates were bought from the manufacturer SPI [26]; some of which had the dimensions 10 x 10 x 1mm. Also some more 20 x 20 x 1 mm were bought, which could be cut into 10 x 10 x 1 mm pieces. However graphite cannot be easily cut clean through. Using a diamond saw causes a graphite substrate to uncontrollably split into several pieces. A sharp knife on the other hand doesn't cut easily through graphite, but instead pushes and grinds away some of the materials. This leads to upstanding ridges at the back of the sides that were cut, which later makes it difficult to use a photo mask.

There are several ways to produce graphite, but substrates of such sizes are usually made by decomposition of for example ethylene onto a surface, though other molecules like ethane, propane and cyclohexane also work [27]. At a local (atomic) level these HOPG-substrates are indeed almost flat, but on a microscopic level they are not. The different HOPG-substrates have different surface structures, which can be seen in figure 3.2.1. The difference in surface structure also affects fabrication results. The lift-off of the samples in figure 3.2.1a and 3.2.1b for example went flawlessly, while the exact same fabrication procedure performed on the sample shown in figure 3.2.1c, removed all ferromagnetic material from the graphite (but not from the SiO<sub>2</sub>).

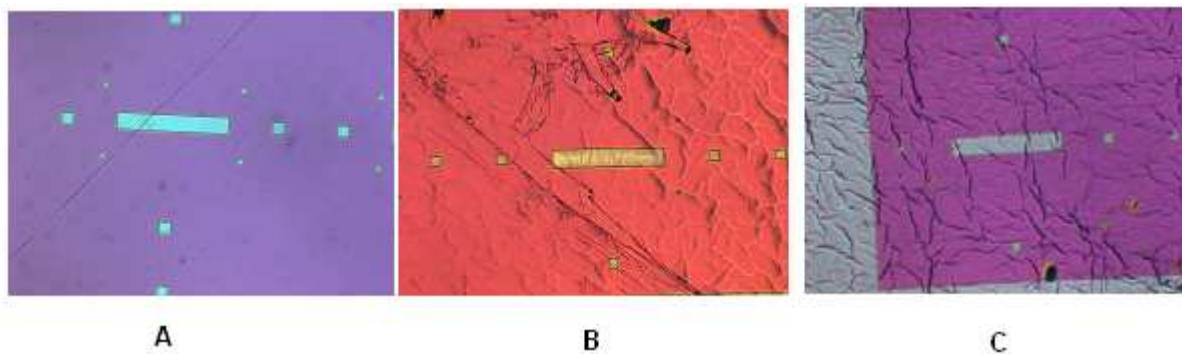


**Fig. 3.2.1:** Optical microscope images of a small selection of different surface morphologies. Note that these images do not show the graphite directly, but use the SiO<sub>2</sub> layer for added contrast. **(a)** A very flat surface with a peeling line defect. **(b)** Slightly sloping surface with major defects locally. **(c)** Very hilly surface.

The binding forces between the individual sheets of graphite are weak, so the topmost layers of HOPG can easily be removed. This fact can be exploited by using Scotch tape to take off the entire top-layer of the graphite, making the sample surface a bit more uniform. In this way the surface structures and defects are usually not removed, but loose patches of graphite can be peeled off. This peeling process is not straightforward, but after a lot of attempts sometimes a good surface can be obtained, though it is never perfect. When peeling an entire top-most layer off the substrate, because of the uneven distributed force on the small sheet of peeled graphite, the sheet usually

breaks along the peeling direction, leading to trenches like the one seen in figure 3.2.1a. The peeling procedure can also be used to remove deposited layers, thus allowing HOPG substrates to be reused, but each time shrinking in thickness. After finishing the peeling, the HOPG substrates are placed for a short while in an ultrasonic bath in order to remove loose patches of graphite. These loose patches might otherwise unpredictably disconnect from the surface during later fabrication steps, which would result in the loss of surface structures.

Overall it can be said that the surface defects, the roughness, different surface morphologies and constantly shrinking thicknesses of the substrates upon repeated peeling steps, result in a highly inhomogeneous surface and unpredictable results with later fabrication steps.

### 3.3 Contact patterning

In this section, the three ways that were used in this work for patterning structures on the graphite surface will be discussed. Note that with both lithography methods a similar structure (lateral device) was made, whereas the shadow mask technique was used to create a different structure (vertical device). Details of the fabrication processes can be found in appendix A and examples of some of the used masks can be found in appendix B.

#### Photolithography

Optical lithography was the starting approach for patterning the substrate. Photolithography was used because the tools for optical lithography were freely available in the cleanroom. Also, in contrast with shadow mask deposition, UV-photolithography can provide feature sizes down to 1  $\mu\text{m}$ , which is a requirement for non-local devices.

After removing the substrate from the ultrasonication bath, a photoresist layer is spun on top of it. The photoresist TI-35ES [28] was chosen for this purpose, since it was the only resist suitable for a lift-off operation that is readily available in the MESA+ cleanroom. Two features make it attractive as a lift-off resist. First of all it has an undercut, which, during the later deposition, enhances the natural shadow-effect. Second it is a relatively thick resist (3.5  $\mu\text{m}$ ), so lifting-off a relatively thick layer is a possibility. In figure 3.3.1, a schematic diagram of the general lithography process of TI-35 is depicted. The precise recipe can be found in appendix A, which was adapted (with minor changes) from a recipe used by an earlier master thesis in the NE-group [29].

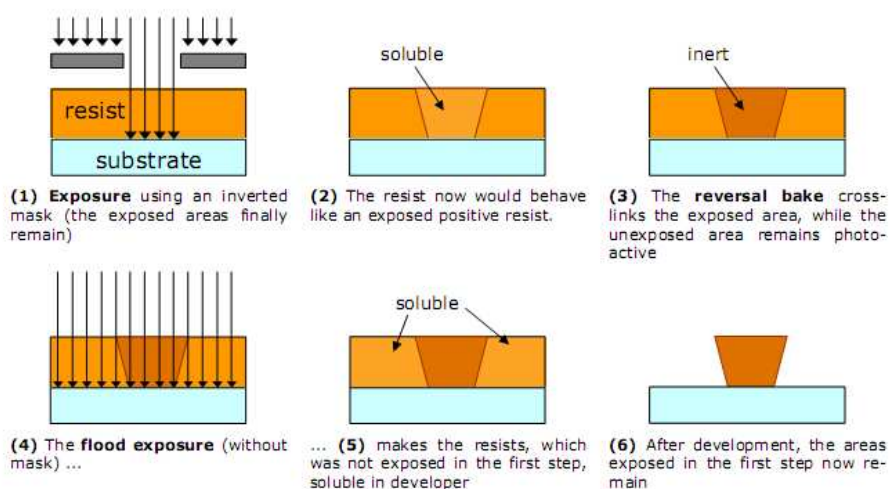
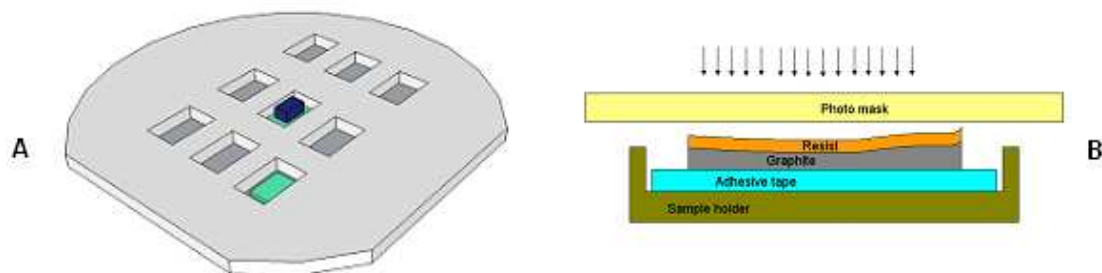


Fig. 3.3.1: Schematic diagram of the steps involved in using the photoresist TI-35 [30].

After having spun the photoresist, the photoresist is baked for a short while in order to harden out. Next is the first exposure, during which the small graphite substrate is placed in a wafer-sized sample holder. The substrate is fixed in a cavity of this sample holder by layers of adhesive tape at the bottom (figure 3.3.2). These adhesive tape layers also serve to bring the surface of the substrate at approximately the same level as the sample holder's. A photo mask is placed very tightly on top of the photoresist and the photoresist is illuminated by UV-light through the openings in the photo mask for a brief period of time, thus defining the pattern. Ti-35 is an image reversal resist, meaning that the parts of the photoresist that were exposed to the light during the first exposure will remain after development. The first exposure dose (together with the later development time) determines the eventual undercut of the photoresist. A lower exposure dose typically yields a stronger undercut.



**Fig. 3.3.2:** Schematic drawings of (a) sample holder, (b) sample holder with respect to the position of the photo mask and the substrate.

After a brief waiting period in order to allow for the out gassing of  $N_2$  out of the photoresist, the resist is again baked. This reversal bake serves to crosslink the polymers in the previously exposed areas of the photoresist, making these parts resistant to both the developer and exposure to light. Afterwards the sample is again, this time without a photo mask, illuminated during a flood exposure. This flood exposure step serves to make the previously unexposed areas soluble to the developer. After the flood exposure, the photoresist is developed using OPD 4262 (standard developer), thus revealing the negative, reversed image of the photo mask.

One of the problems in this master thesis was to obtain a high enough resolution to define a pattern on graphite. With the photolithography facilities in the cleanroom feature sizes of 1-2  $\mu\text{m}$  can be achieved at best. However the distance between the two smaller contacts in the lateral devices ought to be 2  $\mu\text{m}$  or less, so obtaining the maximum resolution was absolutely paramount. The most critical step in the fabrication process is the first exposure, and more specifically the approach and placement of the photo mask. Failure to limit the distance between a photo mask and the underlying sample to a uniform and absolute minimum, leads to a noticeable reduction in resolution due to diffraction effects.

The graphite samples had a rather rough surface on a large scale and some graphite substrates had upstanding ridges, because of earlier cutting. Moreover, graphite substrates were constantly being reused by peeling off a part of their surface, thus constantly varying the thicknesses of all substrates. Placing and aligning a photo mask on these kinds of surfaces proved to be quite difficult. This often resulted in unusable substrates due to the ill defined ferromagnetic contacts or unexpected surface features because of damage to the resist during aligning. These difficulties led us to try using e-beam lithography instead, because of its higher resolution and because it does not need a photo mask. However, that technique turned out to have problems of its own in the fabrication process.

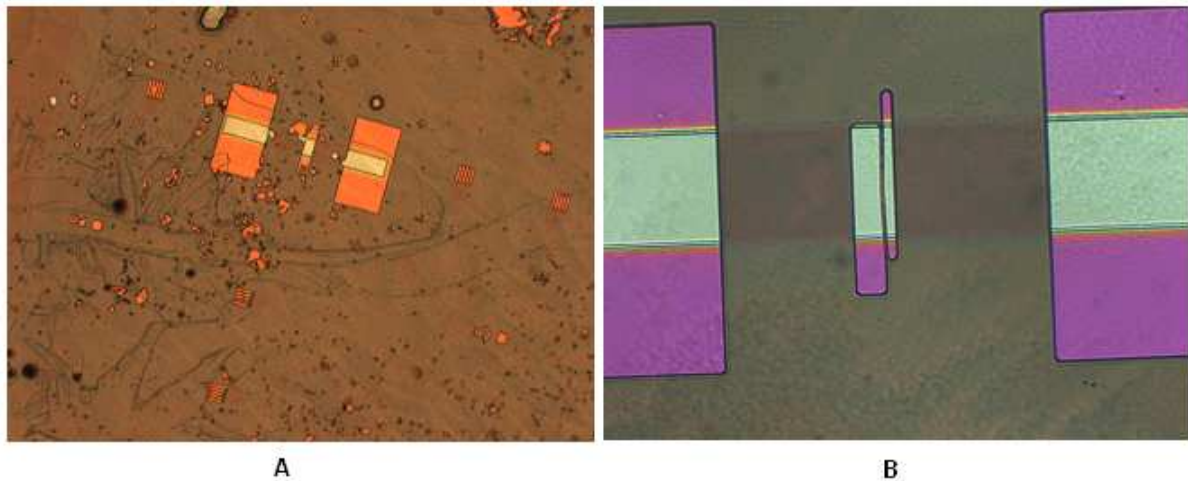


**Fig. 3.3.3:** Optical microscope images of two common photolithography problems. **(a)** Holes in the photoresist likely caused by depositing graphite flakes on the photo mask during aligning. **(b)** Curved photo resist in between the two future smaller contacts probably due to excess undercut. Excess undercut might also be the cause for some of the observed resolution problems. Some thin, undercut lines of photoresist could break, resulting into two smaller contacts without a separation wall.

Eventually however a few “tricks” and adaptations in fabrication process were made by which photolithography became more reliable, though at times still unpredictable. The photo mask was modified to have a variety of contact distances ranging between 2-5  $\mu\text{m}$ , thus always yielding some usable devices. Furthermore, before starting the fabrication process, each sample was measured at three different points in order to assess its thickness. Depending on the measured thickness a number of layers of tape (60-80  $\mu\text{m}$  each) were placed underneath the sample in the sample holder. During fabrication of a sample three photolithography steps had to be done, while only the second (the ferromagnetic contact) was critical in resolution. The first lithography step (defining the channels) thus often served as a test run for the number of layers. One of the final modifications to the fabrication process was to increase the first exposure time from 20 to 24 seconds, to increase resolution and to prevent problems suspected to be caused by excess undercut (see figure 3.3.3b). These measures led to contact distances of 3  $\mu\text{m}$  being quite regularly made, some 2.5  $\mu\text{m}$ , and 2  $\mu\text{m}$  being rare.

### E-beam lithography

E-beam lithography was briefly considered as an alternative to photolithography. The two main reasons being its superior resolution (120 nm on graphite) and because no photo mask is required. However e-beam lithography is a writing technique and thus the time required to write a pattern is quite long. Therefore only the second lithography step (the ferromagnetic contacts) was done by e-beam writing, since the other two could be done quite easily with photolithography.

For e-beam lithography PMMA was used, which is a positive photoresist, meaning that the exposed areas become soluble. This photoresist is spun on the sample and then baked. Subsequently the sample is put in a vacuum chamber and locally exposed to a stream of electrons. The exposure of areas is done in square blocks of 100  $\mu\text{m}$ , which are “stitched” together. The fact that e-beam writing uses a stream of electrons both to write and to inspect a pattern requires that the layers of resist are typically thin (in our case 100 nm). Afterwards the PMMA layer is developed with MIBK as a developer chemical.

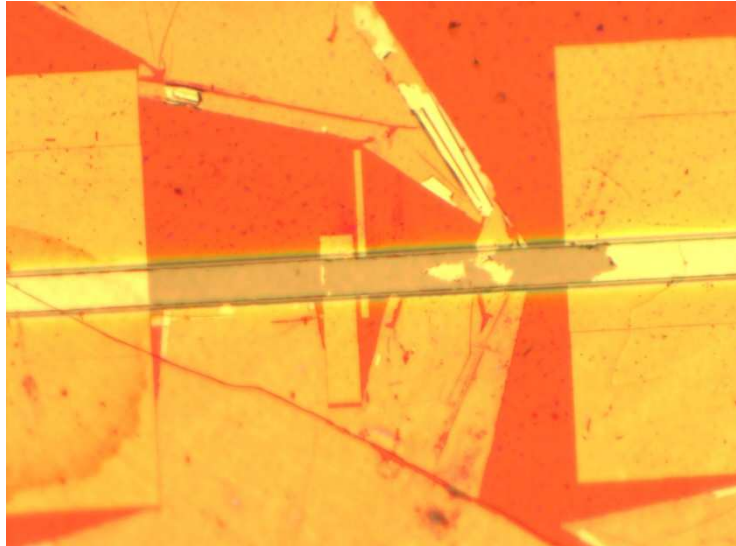


**Fig. 3.3.4:** Effects of acetone soak and 90 seconds of ultrasonication on the contacts. Also note the stitches in the two big contacts.

The results of the e-beam writing on graphite were good, though there was a problem with the stitching in the two big contacts, which could possibly be remedied by later depositing the contact pads over the gaps. The achieved resolution easily exceeded that of photolithography: patterns of contact distances of 1  $\mu\text{m}$  were made. However the problems with the e-beam approach were encountered when doing the lift-off, since PMMA is not a photoresist particularly suited for lift-off. It does not have an undercut and because of its thickness (100 nm) only thin layers can be deposited. A ferromagnetic stack of in total only 12 nm thick was deposited ( $\text{Al}_2\text{O}_3$ , Co, Au 1, 10 and 1 nm respectively thick). Several methods of removing this very thin layer were tried, but none of these could remove the layer without causing major damage. The lift-off problems were probably caused by depositing under an oblique angle, but no additional attempts were made to resolve this. E-beam lithography was thus discontinued because of this lift-off problem, but also because it was perceived that layers of about 10-30 nm would not be a very robust building block.

### Shadow mask deposition

Shadow mask deposition was used to pattern the alternative vertical spin devices of graphite, since it proved to be difficult to create the originally intended lateral spin devices by the two previous methods. The resolution of this technique is mainly determined by the way in which the shadow mask is fabricated. In our case a laser cut an array of rectangles (2.3 x 1.5 mm) out of a thin steel plate; a technique that has a possible minimum feature size of several hundreds of micrometers. The exact shadow mask can be seen in appendix B.

During the first deposition a ferromagnetic stack is deposited on the graphite substrate without a shadow mask. After that the ferromagnetic stack, along with some graphite layers is peeled off the substrate with scotch tape and is attached to a silicon substrate. Afterwards, another ferromagnetic stack is deposited on the former backside of the original ferromagnetic stack using the shadow mask. The shadow mask defines the transferred pattern by blocking the deposition everywhere except at the openings. To prevent accidental deposition from the sides, the shadow mask and the substrate are pressed tightly to each other.

Peeling off the ferromagnetic stack and some graphite layers proved to be the most critical part of this process. Since these peeled off layer is very thin, they are prone to break during the peeling, resulting in some open gaps in the layers. It would be undesirable to have such a gap underneath a contact; minimal contact sizes were therefore preferable to increase the chance of having contacts without such a gap. However during later electrical measurements, problems were encountered, which were thought to be tied to these gaps. For this reason and for the fundamental measurement limitations of the vertical device structure, attempts at shadow mask deposition were halted in favor of lateral devices.

### 3.4 Deposition and lift-off

The general process flow for a lift-off operation is depicted in figure 3.4.1. After having applied a photoresist layer, it is illuminated and developed. Afterwards a layer is deposited on top of the photoresist. The photoresist TI-35 has an undercut after developing, which aids the lift-off by enhancing the natural shadowing effect of the photoresist layer during deposition. The remaining photoresist is subsequently removed by dissolving it in acetone. Because of the shadow-effect during deposition, there should, in principle, be little or no material connecting the layer of deposited material that was formerly on top of the photoresist and the one that was deposited directly unto the sample. Since this connection is non-existent or very thin, the obsolete deposited layers could in principle be removed easily by applying a modest force through for example ultrasonication, leaving the desired pattern intact.

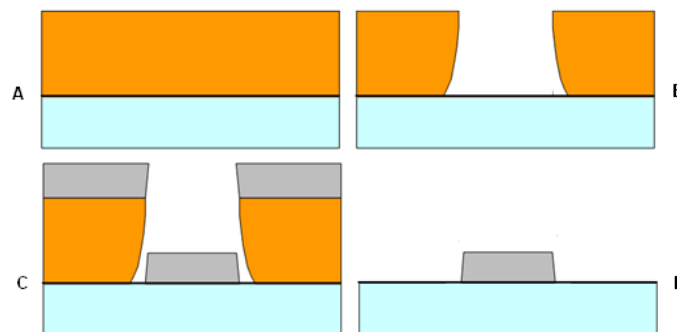


**Fig. 3.4.1:** Schematic diagram of lift-off process used for creating a lateral device. **(a)** Photoresist as applied. **(b)** Developed photoresist with undercut. **(c)** Deposition of material on photoresist. **(d)** Lift-off of the material, leaving behind the desired structure.

However in the early fabrication runs it was observed that using a modest force did not suffice to separate the obsolete layers from the surface. A remedy for this would have been to apply more force instead, an approach often used with silicon samples, but this was not a viable option in the case of graphite samples. Since graphite is not robust and has low surface adhesion, the graphite substrate itself or some of the more delicate patterned features were often damaged, before the lift-off was totally completed. Therefore, during the earlier fabrication runs an unpredictable trade-off was made between local damage to the sample and the amount of lifted-off area in the hope that a sufficient amount of devices survived on a single sample to be usable.

Eventually, the faulty line in the previous reasoning was realized: the assumption is that material is deposited perpendicular with respect to the sample's surface. Depositing material however from an oblique angle leads to a different situation, which is schematically depicted in figure 3.4.2.

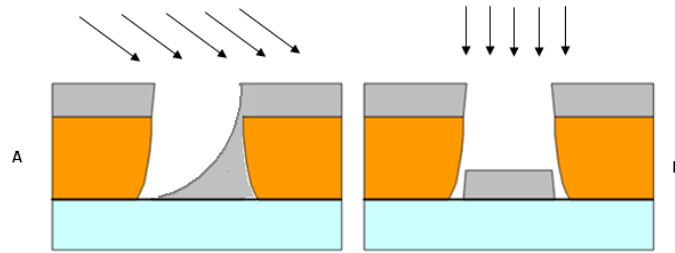


**Fig. 3.4.2:** Schematic drawing of deposition (a) under an oblique angle (b) perpendicular to the substrate.

Depositing under an oblique angle can create on one side of the opening in the photoresist a firm connection to the obsolete layer, while on the other side an enhanced shadow effect is created. This enhanced shadow effect can in principle be seen, when observing from a perpendicular viewpoint.

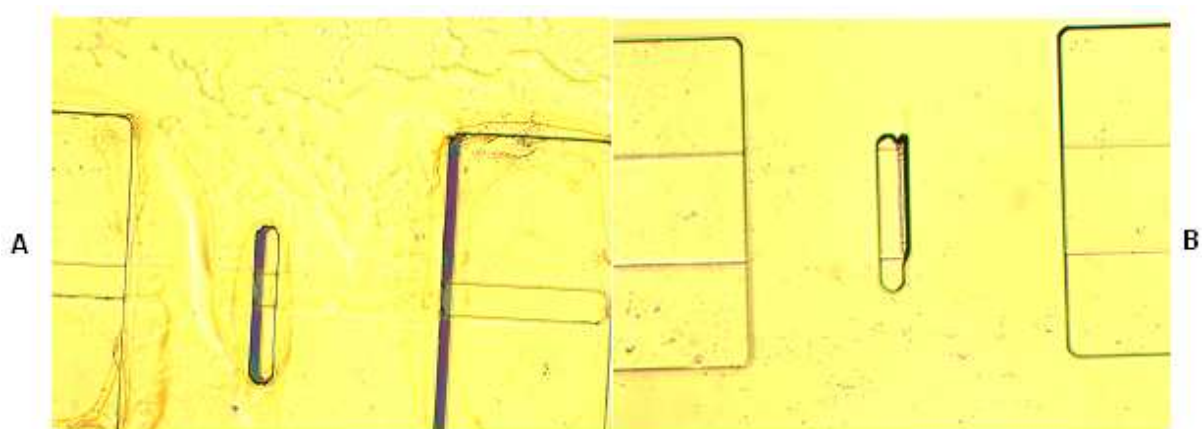


**Fig. 3.4.3:** Shadow effects observed when depositing from (a) an oblique angle (b) a more or less perpendicular direction.

Shadow effects were indeed observed after the deposition of the ferromagnetic stack as can be seen in figure 3.4.3a, but were not directly observed when depositing the  $\text{SiO}_2$  and the contact pads. The absence of the shadow can be explained by the difference in deposition conditions. During the deposition of the ferromagnetic stack the sample is fixed with respect to the source, while in the two other cases the sample is rotating. Using a different sample position for depositing the ferromagnetic stack removed the shadow effect as can be seen in figure 3.4.3b, which resolved most of its lift-off problems. The lift-off problems for the contact pads were resolved by using different materials, which allowed it to be deposited in the same apparatus as the ferromagnetic stack. This could not be done for the  $\text{SiO}_2$  deposition, but its lift-off was found to go far easier as an unintended consequence of modifications of its sputtering equipment during maintenance.

The remainder of this section is divided into three subsections in which the details of the deposition and lift-off of each material stack will be discussed. Since each of these materials stack had different challenges and related phenomena, it is fruitful to discuss them separately.

### Silicon Dioxide

For the first lift-off process  $\text{SiO}_2$  is deposited as an insulating layer; a material often used for such a purpose. In case of a Si substrate a high quality layer of  $\text{SiO}_2$  can be thermally grown, but for a graphite substrate only deposition is available.

SiO<sub>2</sub> is deposited using a homemade sputtering system (TCoater). Several samples are put in a wafer-sized holder, which is placed in the TCoater's chamber at 44 mm from the SiO<sub>2</sub> target. After having pumped down the chamber, it is subsequently filled with Argon gas up to a pressure of 0.004 Torr. A plasma can be generated by applying a magnetic and electric field, which deposits the SiO<sub>2</sub> from the target unto the samples. In this case an RF instead of a DC field has to be used, since SiO<sub>2</sub> is insulating and would thus prevent continued sputtering by charging. A total layer of roughly 500 nm was deposited at an approximate rate of 8 nm/min. The height of this layer rises abruptly with 175nm at the edges; afterwards rising steadily to the total of 500 nm.

One of the peculiar things was that some samples were dotted with discolorations, as can be seen in figure 3.4.4. These discolorations were not observed on bare graphite, but only on the places where a layer was already deposited. These dots were in most cases only observed on places with an underlying SiO<sub>2</sub> layer.

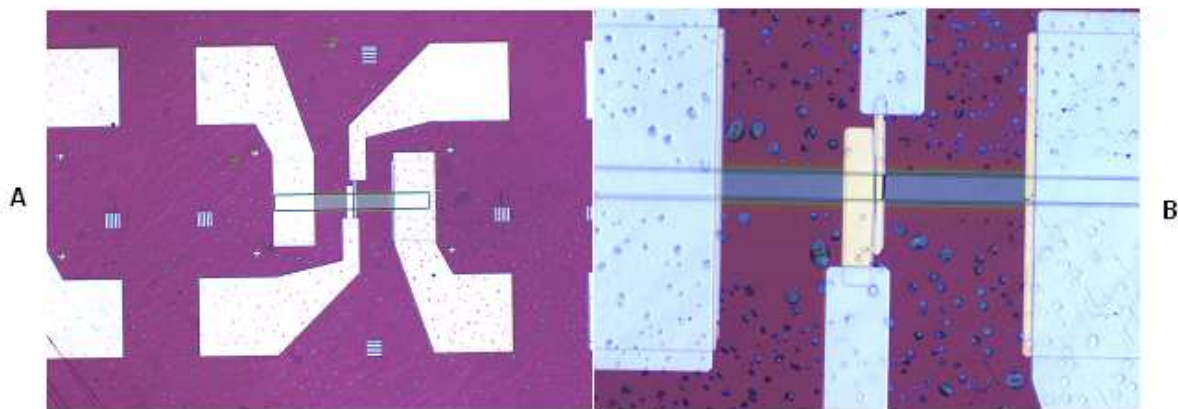


**Fig. 3.4.4:** SiO<sub>2</sub> surface dotted with discolorations. (a) Wide view, showing the almost uniform distribution of the dots. (b) Close up, showing the different sizes of dots.

The dots were also briefly studied with an AFM. As can be seen in figure 3.4.5, the dots are actually mounds. Only a small number of these mounds have been studied, but their heights seem to be ranging roughly between 150 and 300 nm.

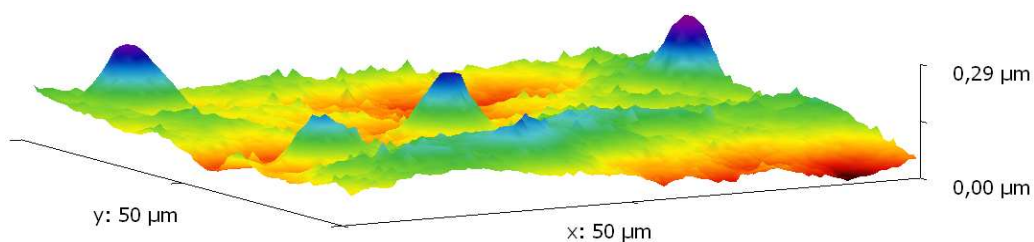


**Fig. 3.4.5:** AFM tapping mode images of the observed discolorations.

The cause for the formation of these types of mounds was not elucidated, but excessive heating seemed to increase their number. It was however suspected that their formation could be originating from absorbed droplets of fluid within the HOPG substrate. Thermal expansion of this fluid, combined with the low adhesion between deposited layer and the graphite, could possibly have led to local release of strain by delamination of the SiO<sub>2</sub> layer from the graphite at the weaker points, leading to the formation of these kinds of mounds.

As was discussed in the previous paragraph a proper and gentle lift-off was essential during fabrication, since a problematic lift-off would render a lot of devices on a sample unusable. An example of damage sustained during one of these lift-off operations can be seen in figure 3.4.6.

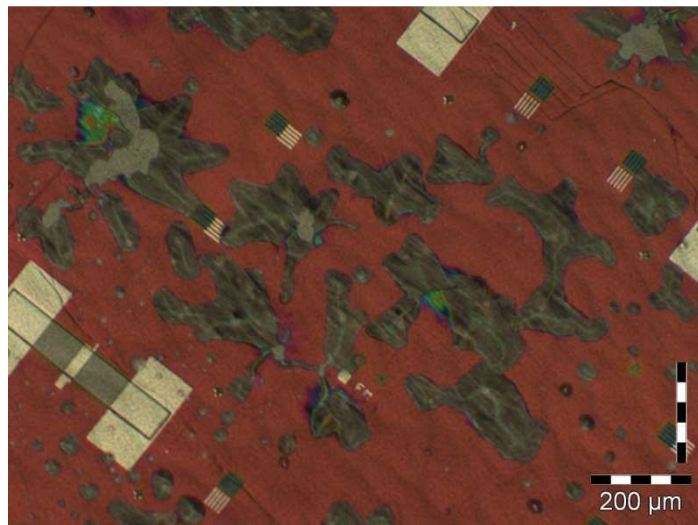


**Fig. 3.4.6:** Damage sustained to the SiO<sub>2</sub> layer during ultrasonication.

In figure 3.4.6 two types of damaged areas can be distinguished. On the one hand there are the grey areas. Here, the deposited layers have been totally removed and the graphite is laid bare. On the other hand there are areas surrounding the previously mentioned category, that have roughly the same height as the undamaged areas, but do have a distinct color compared to the undamaged areas. Inspection with AFM indicated that these areas consist out of SiO<sub>2</sub> that is still partially attached to the undamaged areas and also slightly tilted.

The earlier mentioned mounds could also be related to this ultrasonication damage. One sample without any observable dots was placed in an ultrasonic bath for several minutes without sustaining major damage, while other samples already displayed damage after ultrasonication for less than a minute. It can be reasoned that these mounds function as weak spots, being more prone to break during ultrasonication, because of them missing a direct mechanical contact to the underlying substrate.

The problem of the lift-off of the SiO<sub>2</sub> layer was eventually largely solved, probably partly as an accidental consequence of maintenance of the TCoater. Additionally the adhesion between the graphite and the SiO<sub>2</sub> was significantly better than in the case of the other materials, making it a less troublesome lift-off than in the case of those materials.

### **Ferromagnetic stack**

The ferromagnetic stack was deposited using a DCA M600 metal/oxide MBE system, an e beam evaporation system owned by the NE-group itself. The samples are put in a sample holder, which is subsequently placed in a UHV chamber (10<sup>-10</sup> Torr). Under an electric field of several kilovolts, electrons accelerated after being emitted from a hot filament through which a current is sourced to achieve a set emission current. These accelerated electrons crash into a target, containing the material to be deposited, thus heating it up. To prevent excited (heavy) ions from this target to travel back to the filament, the acceleration path from the electrons is curved by a permanent magnet. Continued heating causes the target material to become liquid, to evaporate and subsequently to

deposit unto the surface. A low pressure is maintained during deposition by a liquid nitrogen cooled baffle. The deposition rate can be very accurately monitored by a vibrating quartz-crystal, while the deposition itself is stopped and started by opening/closing a shutter. In principle the DCA also has the ability to do shadow-mask deposition, which was used in the case of the vertical spin devices.

Au (50 nm)	Au (100 nm)			Au (3 nm)		
Cr (30 nm)		Al (130 nm)	Al (100 nm)			
Au (50 nm)			Au (3 nm)	Au (50 nm)	Au (3 nm)	
					Al (50 nm)	Al (3nm)
Co (50 nm)						Co (100 nm)
Al <sub>2</sub> O <sub>3</sub> (1 nm)			Al <sub>2</sub> O <sub>3</sub> (2 nm) (Rotating deposition)			

**Fig. 3.4.7:** Composition and thicknesses used for the ferromagnetic stacks and contact pads of different samples.

The first of these layers to be deposited is the tunnel barrier. A layer of 1-2 nm of Al<sub>2</sub>O<sub>3</sub> is used for this purpose. Al<sub>2</sub>O<sub>3</sub> is known to have a high degree of uniformity and flatness, making it a suitable material for research. In order to create an Al<sub>2</sub>O<sub>3</sub> tunnel barrier the usual method is to deposit Al and to subsequently plasma oxidize it. However, this is not suitable when using a HOPG substrate, so instead Al<sub>2</sub>O<sub>3</sub> is deposited directly. To remove any remaining oxygen vacancies in the Al<sub>2</sub>O<sub>3</sub>, the sample is naturally oxidized in pure oxygen (100 mTorr) in the adjacent loadlock of the DCA. These oxygen vacancies could otherwise create defects, which would prevent the tunnel barrier from properly functioning. The next layer to be deposited is the ferromagnetic material; in our case cobalt was used. To prevent cobalt from oxidizing, an additional capping layer is deposited directly unto it. For this capping layer different materials were used: gold, aluminum or a combination thereof. Throughout the project different compositions and thicknesses of these stacks were used in order to improve the yield/performance of the fabricated devices. A schematic of the different thicknesses and compositions can be seen in figure 3.4.7.

The lift-off procedure used for the ferromagnetic stack was similar to the one described for SiO<sub>2</sub> (see above). The developed photoresist TI-35 underneath the deposited ferromagnetic stack was dissolved in acetone and a very brief and mild ultrasonication could remove the remaining excess material. However, in comparison with the SiO<sub>2</sub> lift-off, the conditions for the ferromagnetic stack were a bit different. Before realizing the problems caused by oblique deposition, lift-off was difficult to achieve and was attempted by extending the ultrasonication time. Often this would result in all ferromagnetic material (including the contacts) being removed from within the channel, before any significant portion of the ferromagnetic stack on top of the SiO<sub>2</sub> would be removed. This led us to conclude that the adhesion between the ferromagnetic stack, presumably the Al<sub>2</sub>O<sub>3</sub>, and the graphite was very weak. This fact, in combination with the small, fragile ferromagnetic contacts often led to one of the smaller contacts (or both) breaking (as can be seen in figure 3.4.8). Since these two contacts were crucial for doing non-local and Hanle measurements, this problem significantly reduced the yield of usable contacts. Eventually this problem was partially resolved by doubling the thickness of the ferromagnetic stack (increasing the capping layer from 3 to 50 nm) and by being able to reduce the ultrasonication time (allowed by perpendicular deposition).

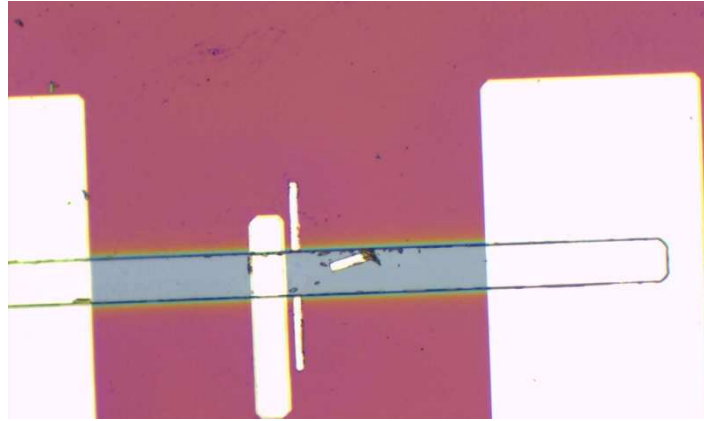


**Fig. 3.4.8:** Breaking of a small ferromagnetic contact after ultrasonication. The broken-off section is still lying in the channel.

A different problem was again related to depositing under an angle. As can be seen in figure 3.4.9, for some samples a shadow image of the ferromagnetic contacts can be seen. This was a major problem, because a part of the shadow contact was not in contact with the tunnel barrier, but directly with underlying graphite. The cause for this lay in the fact that the ferromagnetic stack was deposited with two different e-beam deposition guns, with each having a different position (and angle) with respect to the sample during deposition.

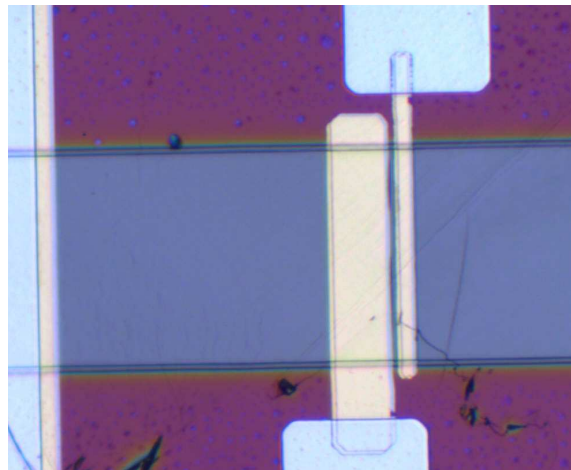


**Fig. 3.4.9:** Optical microscope of a deposition shadow of the ferromagnetic stack.

The problem could not be resolved by a different choice of materials, since  $\text{Al}_2\text{O}_3$  was in Gun 1, and all the ferromagnetic materials were situated in electron Gun 2. Swapping materials between guns is non-trivial, and should be considered only as a last resort, since it will affect all deposition processes in which the DCA is used. One of the ways in which we tried to resolve this was depositing  $\text{Al}_2\text{O}_3$  from four different angles ( $0^\circ$ ,  $90^\circ$ ,  $180^\circ$  and  $270^\circ$ ), thus depositing  $\text{Al}_2\text{O}_3$  in the undercut of the photoresist. This method presumably resulted in a tunnelbarrier of 0.5 nm thick at the edges and 2 nm in the middle, but at least in this way it was ensured that everywhere underneath the cobalt a tunnelbarrier was present. Also Al was subsequently used as a capping layer, since it was located in the same e-gun as the cobalt.

Only after finishing the project an alternative way to resolve this issue was realized. The position, under which deposition under a perpendicular angle occurred, was never directly visually confirmed. Instead it was only confirmed indirectly by trying lift-off for a limited number of samples at different

deposition positions and subsequently assuming that the ones with a proper lift-off had, for all practical purposes, a more or less perpendicular angle with respect to the trenches. Since at that time the thicknesses of  $\text{Al}_2\text{O}_3$  and Au were negligible to Co (1, 3 and 50 nm, respectively), the problems derived from use of two different guns were realized only late in the stage of my project. A fellow master student, Koert Vergeer, determined later the proper deposition positions for both guns. It turned out that I would only have had to turn the sample  $180^\circ$  around for the different guns in order to solve this issue.

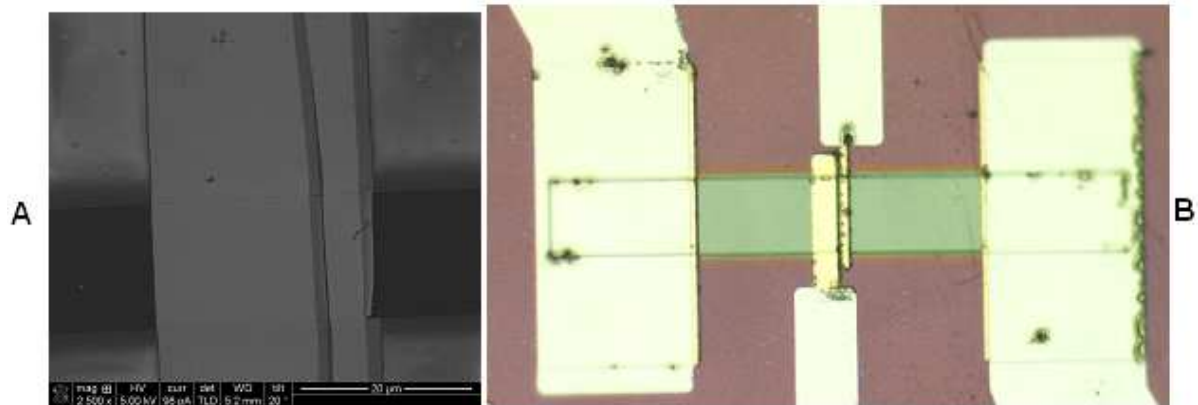


**Fig. 3.4.10:** (a) SEM image of small ferromagnetic contacts with a big deposition shadow. (b) Optical image of contacts presumably with partially oxidized cobalt at the exposed shadow.

The shadowing caused some additional problems. In some devices the lateral displacement by the shadowing effect was so big, that the gap between the two smaller contacts could be bridged. This can be seen in figure 3.4.10a. In addition in the same picture a shadow layer of the right contact is seen to hang partially loose. Additional measurements with the AFM indicated that this was not a rare occurrence. These loose and potentially movable patches could possibly be one of the causes for irreproducible electrical measurements (see chapter 4.2). Additionally, some shadow contacts degraded over time, as can be visually seen in figure 3.4.10b. This is probably the cobalt layer partially oxidizing. This was resolved by using aluminum as a capping layer, since both Co and Al come from the same e-guns.

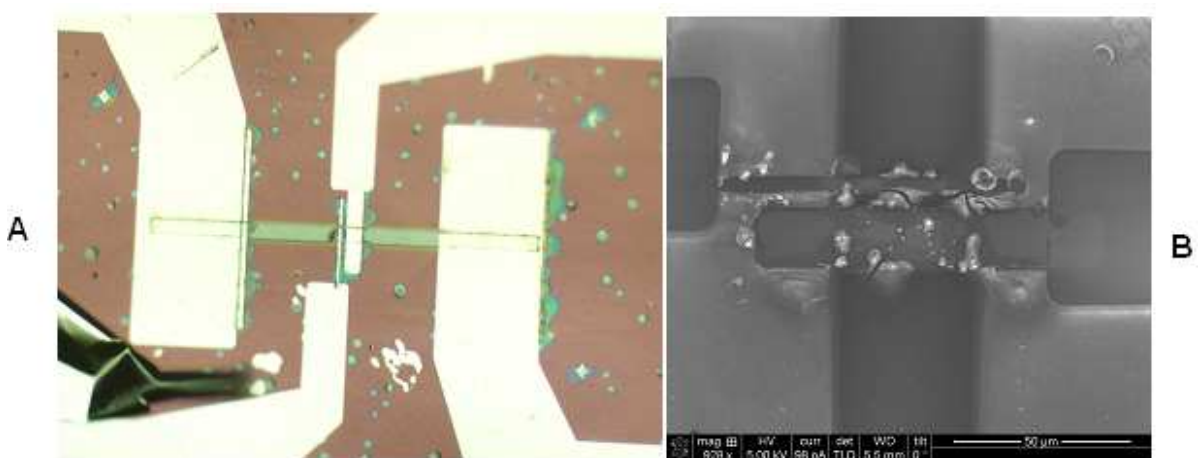


**Fig. 3.4.11:** Deformation around the contacts after exposure to low-temperatures. (a) As seen through an optical microscope. (b) SEM picture of the two small contacts.

In the later contacts yet again a problem surfaced. In order for tunneling to become the dominant transport mechanism, it is necessary to cool down the sample to very low temperatures. While measuring these devices, sometimes, at certain temperatures, signals abruptly decayed into noise and no signal could be observed anymore at this temperature. Upon raising the temperature again, on certain occasions the signals returned at a certain temperature ( $< 230$  K), and an IV-curve could once again be measured. Afterwards the sample was inspected underneath an optical microscope and using the SEM, as can be seen in figure 3.4.11. The discolorations were reminiscent of the dots in  $\text{SiO}_2$ , which were earlier observed (see figure 3.4.4). The SEM image shows a surface, which, especially in the graphite channel, is highly inhomogeneous and wrinkled. Furthermore, in AFM tapping-mode studies, a height and phase difference was observed between the distorted and undistorted areas.

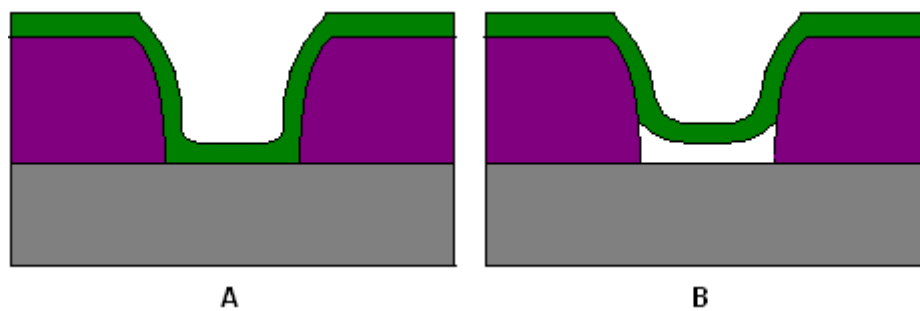


**Fig. 3.4.12:** Schematic drawing of a possible scenario for release of thermal strain in the lateral device. **(a)** At room temperature the ferromagnetic stack (green) is firmly attached to the  $\text{SiO}_2$  (purple) and graphite (grey). **(b)** At low temperatures the ferromagnetic layer ruptures from the graphite substrate, due to the low adhesion to and difference in thermal expansion with the graphite.

A possible cause for the damage sustained during the cooling, might come from using different materials, with different thermal expansion coefficients, for the ferromagnetic stack. Aluminum has the highest thermal expansion coefficient ( $22 \text{ K}^{-1}$ ) of the four stack materials, while graphite has a lateral coefficient of only around  $8 \text{ K}^{-1}$  [31]. It is possible to consider a scenario as sketched in figure 3.4.12, in which the ferromagnetic contact contracts, resulting in losing contact with the conducting graphite. Since it is very difficult to look underneath the ferromagnetic stack, this idea could not be confirmed, but the earlier mentioned observations make it very probable that something mechanical happens during cooling. Trying to overcome this problem we reduced the thickness of the Al layer from 50 to 3 nm and increased the Co layer thickness to 100 nm. Since cobalt has a thermal expansion coefficient of about  $12 \text{ K}^{-1}$  [31], it was thought this could resolve the problem. However, during lift-off of the ferromagnetic stack most contacts were destroyed in the channel, while remaining intact on top of the  $\text{SiO}_2$ . As of yet this problem remains unresolved, since no time was left to do additional deposition runs.

## Contact pads

As was discussed in chapter 3.1, the contact pads served as conducting conduits to later connect the fabricated devices via wirebonding with external measurement apparatuses. Originally gold was used as the main conducting material, with chromium serving as an adhesion layer to improve the connection between the gold and the underlying substrate. This stack was deposited using the system "Sputterke". This is a sputtering system, which works in a similar manner as the TCoater (see above). Via a loadlock samples are put in a deposition chamber, which is pumped down and subsequently filled with Argon gas to a pressure of 0.66 mTorr. By applying a magnetic and electric field argon gas is turned into plasma, from which ions are accelerated towards a target, in turn sputtering atoms (and ions) from that target. These atoms can deposit on the samples, with deposition being timed by a manual shutter. The deposition rate for gold is typically is around 50 nm/min; the actual rate scaling more or less linearly with applied power. Sputterke can hold three targets, allowing for deposition of three different materials in a run.

As stated, gold and chromium were originally used, but over time the materials and thicknesses were varied (see figure 3.4.7); the reasons for this often being lift-off and/or problems with the wire bonding. In comparison with the two earlier lift-off layers, the lift-off problems of the contact pads layers were much less severe. The reason for this lay partly in the fact that its exact features were of far lesser importance and did not transfer to another future layer.

The original gold layer of 50 nm thick was quickly scaled up to 100 nm, when it proved to be too prone to damage during wire bonding. This was also the reason for the transition to an aluminum layer, since it was speculated to be sturdier and moreover did not need a Cr adhesion layer. This transition also turned out handy later, when it was realized that the lift-off problem derived from oblique angle deposition. This problem was however not earlier observed, since the samples rotated during deposition in Sputterke, masking any shadow effect. Thereafter the contact pads were also deposited in the DCA (described above). Since Cr was unavailable in this machine, using gold as a main material for the contact pads was no longer possible. However gold was later again added as a capping layer to the aluminum, to rule out the possibility that the many non-functioning contacts were caused by an oxide layer on the aluminum contact pads.

## 3.5 Wire bonding

The final problem of using a graphite substrate was connecting the devices to the measurement equipment. For other kinds of substrates usually wire bonding is used; by pressing a gold or aluminum wire with a wire bonder on top of a contact pad, the wire sticks to the surface and thus a robust electrical contact is made. This procedure however does not work well for contact pads with an underlying graphite surface. Usually the wire didn't stick and severe damage is locally created by the pressure. A possible mechanism for this damage might lie in the low adhesion between the graphite and the SiO<sub>2</sub>, leading to certain pressure hotspots, which are subsequently prone to break. A second mechanism, also related to the low adhesion, could be that planes of graphite slide with respect to each other and the SiO<sub>2</sub> layer, resulting in damage. It was attempted overcome the first problem by doubling the thickness of the contact pad, but to no avail. Even in the few cases that the wire did stick, the structural damage caused by the pressure of the bonding process is also present (figure 3.5.1). This structural damage might result in unreliable contacts, which might partially explain the different types of unstable electrical behavior observed using these contacts.



**Fig. 3.5.1:** A device bonded by using regular wire bonding. Notice that the surface of the SiO<sub>2</sub> layer appears to be highly irregular/damaged, which is probably caused by defects in the underlying graphite layer of unknown origin. The spot of the contact pads where the wires were pressed onto has turned from bright yellow to black. The color change indicates that the gold-layer is probably still present, but the loose patches are tilted with respect to the surface. Also notice the grey spots, where all deposited layers were removed from the graphite.

Since putting considerable pressure on the substrate did not turn out to be a viable option, subsequently the approach shifted to using a conductive glue (silver epoxy) [32] to establish an electrical contact. A glue drop was first put on the tip of a wire extending from the wire bonder by sticking it into a reservoir of glue. The glue drop on the tip of this wire was later carefully brushed on a contact pad in order to transfer this drop. After waiting a moment to let the droplet partially dry, a wire could be manually pressed into it. An example of this approach can be seen in figure 3.5.2.



**Fig. 3.5.2:** A device bonded by using silver epoxy. Note that the hole in the upper left contact pad was already pre-existent and does not protrude into the SiO<sub>2</sub> layer. The damage in the right part of the image is caused by breaking a wire at the substrate.

Though the silver epoxy approach leads to better results, there are still some problems associated with it. Usually several attempts had to be made to have the wire remain sticking in the glue; which meant that during the failed attempts, the wires would crash into the surface, spreading some glue and causing damage. Sometimes the bonded contacts got slightly damaged during this type of bonding. It is likely that this was for similar causes as in regular wire bonding. Due to the fact that this damage was subtle, damaged sections could later be covered with silver paste, making it both hard to notice on later optical inspection and possibly creating electrical shorts. Another hazard was the composite nature of the glue. Because the glue was created by mixing two different components, the behavior was not always as expected. Sometimes too much glue was used, which resulted into a glue droplet spreading beyond the boundaries of the contact pad.

Though both wire bonding methods had some difficulties, the silver epoxy method was preferred over the regular wire bonding. Regular wire bonding had a far lower probability of wires sticking to the contact pads and always caused a lot of damage, while in the case of silver epoxy bonding the damage was hardly noticeable or non-existent.

## Chapter 4: Experiments

### 4.1 Experimental methods

Measuring the spintronic properties of materials often requires high magnetic fields and low temperatures. The “Bruker” measurement equipment is able to achieve both. A picture of the Bruker equipment can be seen in figure 4.1.1.



**Fig. 4.1.1:** Photograph of the “Bruker” system. Among its constituent parts are an electromagnet (1), measurement electronics (2), a cryostat containing the sample (3), a temperature controller (4) and a connection to an external helium vessel (5).

A sample is placed in the cryostat (inside sample chamber filled with gaseous helium), which is at the center between the poles of an electromagnet. The electromagnet can generate magnetic fields up to 2 T. By flowing liquid helium around the sample chamber, sample temperatures as low as 5 K can be achieved. The exact temperature is determined by controlling the flow of liquid helium with a valve and by a build-in heater. This heater also allows for sample temperatures up to 350 K. A measurement computer performs the handling of the magnet and Keithley electronics, using a predefined script. A Keithley 6621 is used as a current source and a Keithley 2182 as a nanovolt meter.

The SVT system is an alternative measurement setup that is very similar to the Bruker setup, though its cooling mechanism is different. It is cooled by a closed cycle helium gas refrigerator, which provides sample temperatures as low as 10 K. Its electromagnet can generate magnetic fields up to 45 mT. In the SVT setup, usually a Keithley 2400 is used as a current/voltage source, although the Keithley source/measure units are interchangeable between the two setups. In addition to the Keithley electronics, a lock-in amplifier was used in the later stages of this thesis to decrease voltage noise.

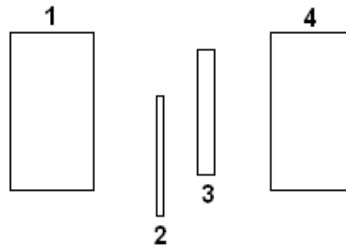


**Fig. 4.1.2:** Number designations of the contacts.

In figure 4.1.2 the number designation (used in this chapter) for the contacts in lateral devices, is shown. However, it was difficult to wire bond all four contacts of a single device. Silver epoxy bonding resulted in less damage to the contact pads than traditional wire bonding (see chapter 3.5), but sticking a wire into the glue on the contact pad and keeping it there, was tricky. When a wire was spanned from the sample holder contact to the contact pad over a long distance, the strain would cause it to eject from the glue drop. This made only a few nearby contacts on the sample holder suitable for wire bonding a particular device. Additionally, a significant ratio of ferromagnetic contacts gave no signal. For these reasons, a lot of measurements used contacts of multiple adjacent devices. If such is the case, it will be mentioned explicitly.

Additionally, another methodological hindrance should be mentioned. The sample holders used for the Bruker and the SVT setups have ten contacts, allowing for (at most) ten wire bonded contacts. Silver epoxy bonding gives strong bonding. However, if the sample holder contact has to be reused, a large area of the contact pad is damaged when removing the epoxy bonded wire. This, together with the recycling of samples for fabrication, made it impossible to measure some contacts again.

## 4.2 Tunnel barrier inspection

The goal of this thesis was to measure both the spin relaxation time and length in graphite. In order to measure these, the Hanle and/or non-local voltage signal needed to significantly exceed the voltage noise. Since both these signals scale with the spin accumulation (equation 8), a high accumulation is necessary in the graphite. Due to the conductivity mismatch between ferromagnets and non-magnetic materials with low densities of states, a tunnel barrier ( $\text{Al}_2\text{O}_3$  in our case) is needed in between [2], [33]. Therefore, the quality of the tunnel barrier needs to be ascertained, before starting non-local probing measurements.

The resistance of the tunnel barrier needs to be high enough to be dominant, but low enough to give sufficient signal. Common defects of tunnel barriers are pinholes (locally thin tunnel barrier regions) and impurities/vacancies, which can e.g. serve as spin-flip sites. Characterization of the tunnel barriers can be done by two-terminal I-V measurements of lateral devices. High quality tunnel barriers give a distinct non-linear I-V curve and should be relatively temperature independent.

However, in the earliest samples, most I-V measurements of contacts showed only white noise. In addition, some contacts did give an (Ohmic) response. However, when measuring these contacts again, they sometimes no longer gave a signal. Among the considered possible causes for this were problems with the initially used wire bonding method or oxidation of the ferromagnetic stack, though the latter was considered unlikely.

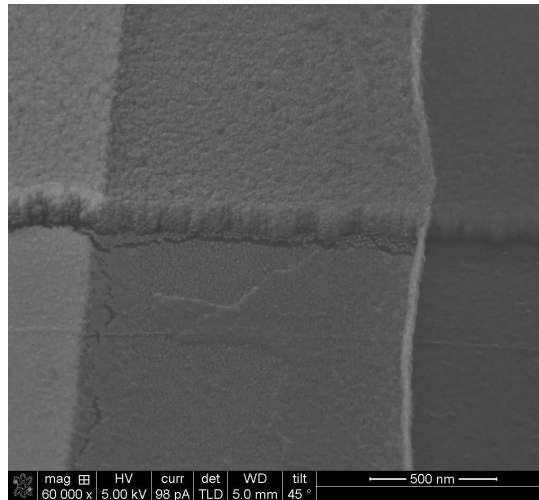


**Fig. 4.2.1:** SEM close up of a ferromagnetic contact lying across the edge of the graphite channel on the SiO<sub>2</sub> layer. On the left side the edge of the proper contact can be seen, while the layer in the center is the shadow image of this layer due to deposition with two e-guns. Cracks in the contacts can be seen at the border between the shadow and the proper contact, and at the border of the graphite channel.

Another possible cause was observed using SEM inspection (see figure 4.2.1). A line of cracks in the ferromagnetic contact could be seen at the steep SiO<sub>2</sub> edge of the graphite channel. It is likely that there was no connection between the lower and upper part of the contact, which would yield no-signal. In cases there was a connection; this could be easily broken, resulting in a no-signal contact. In later fabrication runs, a thicker ferromagnetic stack was used. Using SEM, one could no longer observe any cracks and the ratio of no-signal contacts decreased. Another approach could have been to reduce the SiO<sub>2</sub> thickness, resulting in a smaller step in the SiO<sub>2</sub> layer at the edge (currently 175 nm). This was not attempted. The development of the fabrication process had been a difficult mechanical balancing act with the SiO<sub>2</sub> layer serving as a firm building ground. Drastically changing the thickness of SiO<sub>2</sub> layer could overturn the whole fabrication process development, which would have been difficult to redo in the remaining time of the master thesis.

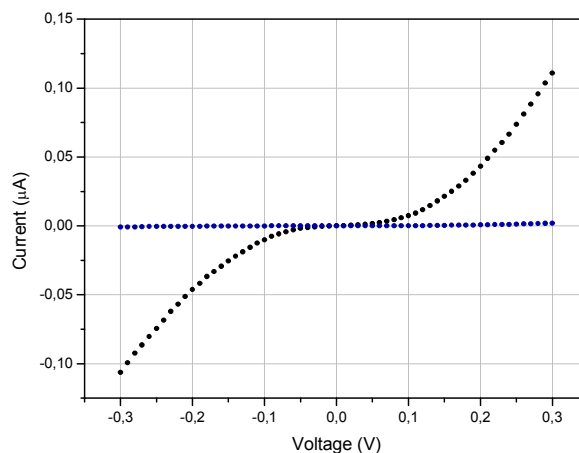


**Fig. 4.2.2:** Equivalent I-V measurements between contact 3 and 2 at 10 K.

Two of the first obtained I-V curves indicative of tunneling as the dominant transport mechanism, can be seen in figure 4.2.2. Both curves show a non-linear response typical for a tunnel barrier. However, both curves have been measured under the exact same conditions for the same contact, though there is an order of magnitude difference in their resistance.

These sudden shifts in resistances in between measurements happened not only frequently for tunneling curves, but also for the more common Ohmic behaving contacts. Resistances suddenly changed for example from  $10^9$  to  $10^3 \Omega$  and behavior could switch from tunneling to Ohmic. The cause for this is unknown. It was definitely not because of damage due to traditional wire bonding, since it still occurred after switching to silver epoxy wire bonding. Possibly, it was also related to the cracks shown in figure 4.2.1. However, it still occurred, though less often and far less severe, after the thickening of the ferromagnetic stack. Aside from the resistance changes, only measurements that included at least one smaller contact (2 & 3) displayed tunnel behavior. This led us to guess that only the smaller contacts could give tunnel behavior, due to its smaller (defective) surface area.

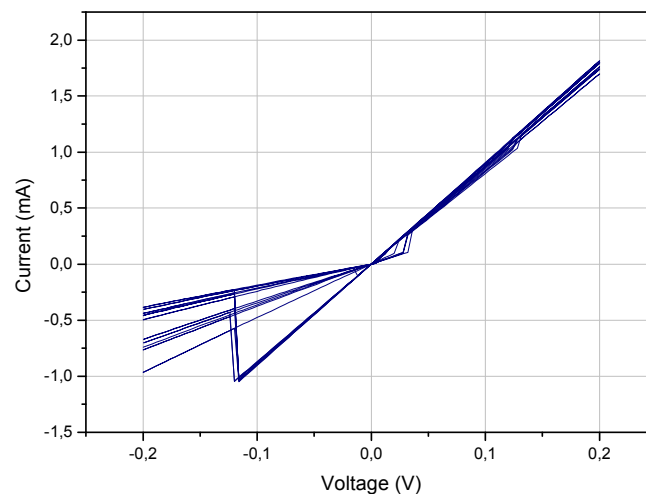


**Fig. 4.2.3:** Sweeping I-V measurement between contact 4 and 2 at 15 K.

The changes in resistance in early samples were never directly observed during I-V sweeps, always occurring in between measurements. However, when sweeping the voltage back and forth from a negative value to a positive value, the curve in figure 4.2.3 was observed in one of the later samples. In the positive voltage domain, resistance is rather stable, but in the negative domain several resistance configurations are possible. At around  $-0.15$  and  $0.025$  V switching occurs between these configurations. A cause of this could again come from the cracks seen in figure 4.2.1. It is possible that a limited number of connections are extending beyond the cracks; loose patches of the electrode stacks at the site of the cracks are perhaps moved by the electric field. This would give a field driven contact (FDC), leading to the behavior seen in figure 4.2.3.

It is possible that the resistance changes like in figure 4.2.2, also originate from this field driven contact phenomenon. However, even after thickening the ferromagnetic stack, smaller resistance changes during (not necessarily FDC) and in between measurements were still observed. One explanation could be that these are at least two different mechanisms at play. While one (the cracks) has been disabled, the other (unknown) one is still at work, causing the unreliability of the tunnel

barrier. An alternative explanation could be that even after thickening the ferromagnet, the crack is still present in one form or another. SEM had difficulty focusing on the step edge and could have overlooked the crack in the thickened ferromagnetic stack, though this is unlikely. However, if the cracks in  $\text{Al}_2\text{O}_3$  are caused by a shadow effect of deposition near the high  $\text{SiO}_2$  step, this problem would be solved by rotational deposition of  $\text{Al}_2\text{O}_3$ .

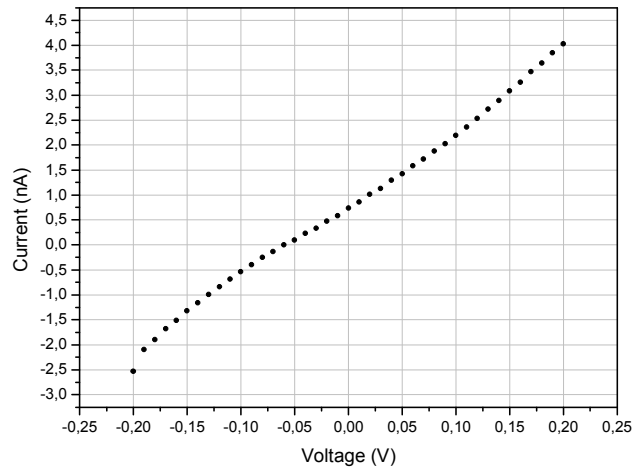


**Fig. 4.2.4:** I-V measurement between contact 4 and 2 at RT (different devices).

Deposition of slightly thicker  $\text{Al}_2\text{O}_3$  from four different angles was implemented almost simultaneously with the thickening of the ferromagnetic stack. It did give a (perceived) higher reliability to the tunnel barriers and significantly higher resistances. One of the better tunnel barrier curves of this new generation of devices can be seen figure 4.2.4, which was measured at room temperature. It should be noted that there is a slight asymmetry in the curve; the measured current in the negative domain is lower than in the positive; something that was also the case in figure 4.2.2.

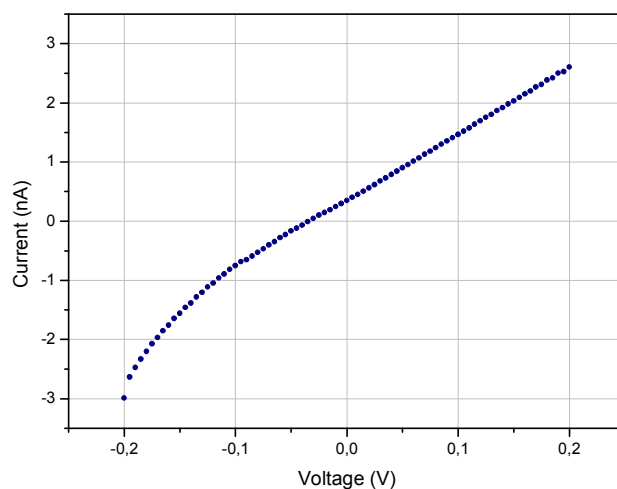


**Fig. 4.2.5 :** I-V measurement between contact 1 and 3 at RT.

In addition to better tunnel barriers, the new innovations yielded some unexpected results. A rather asymmetric I-V curve can be seen in figure 4.2.5. In the negative voltage domain its behavior is non-linear, while in the positive domain it is behaving nearly linear. The slight asymmetry observed in figure 4.2.3 & 4.2.4, could be explained by the asymmetry of the tunnel junction, since the  $\text{Al}_2\text{O}_3$  tunnel barrier itself is asymmetric, being contacted by two distinct materials on each side (graphite and Co, respectively). However, the asymmetry observed in figure 4.2.5, likely has a different (unknown) origin.

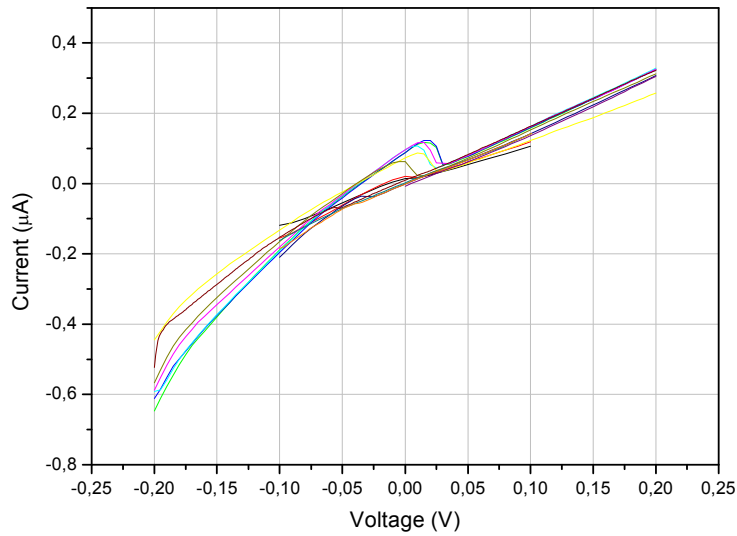


**Fig. 4.2.6:** Equivalent I-V measurements between contact 4 and 1 at RT.

In addition to this asymmetry, some contacts gave odd curves. The contacts used in figure 4.2.6 and figure 4.2.7 are the same; the only difference between the two graphs is the reversed polarity. In figure 4.2.6, a current bulge can be observed, which is more or less reproducible, while it is absent in figure 4.2.7. Both graphs show a non-zero current at zero voltage, which is indicative of capacitive behavior. However, it is not known where this parasitic capacity could come from, but a possible origin could be movable ions/oxygen vacancies in the  $\text{Al}_2\text{O}_3$  dielectric.

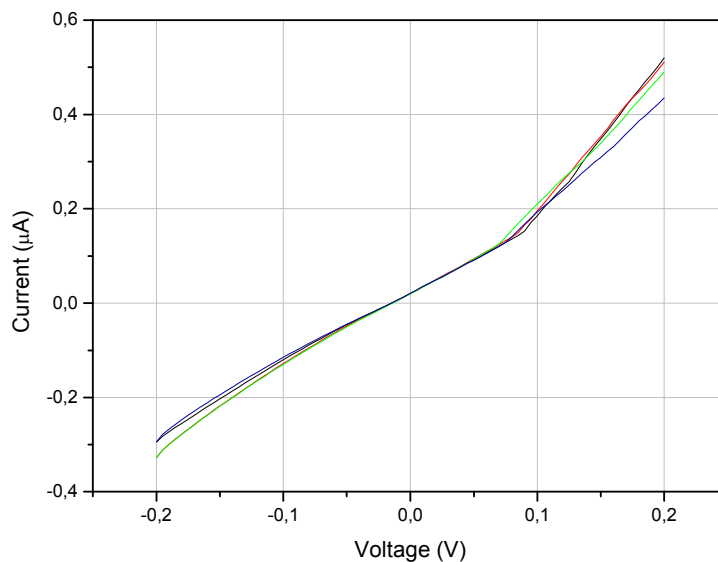


**Fig. 4.2.7:** Equivalent V-I measurements between contact 1 and 4 at RT.

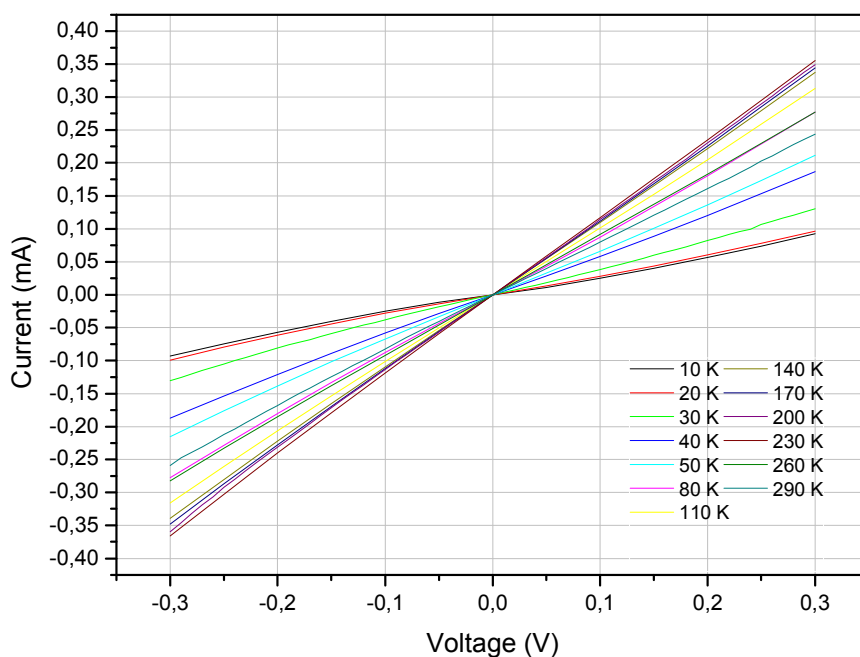


**Fig. 4.2.8:** V-I measurement between contact 4 and 3 for a range of different temperatures. The resistance curves at 290 and 260 K deviate from the general temperature dependence trend, but this is attributed to tunnel barrier instability.

Tunneling through a tunnel barrier is nearly temperature independent. Therefore, the resistance of a proper tunnel barrier should be only weakly dependent on temperature. The resistivity of bulk graphite decreases at low temperatures, but the total resistance of the device in figure 4.2.8 increases instead. Therefore, this increase in resistance can be mostly attributed to the tunnel barrier. It is possible that oxygen or other types of vacancies are present within the  $\text{Al}_2\text{O}_3$  layer, which could lead to thermally activated defect-assisted tunneling. These vacancy states, presumably having energy levels just below the barrier energy, are filled at low temperature. However, at higher temperatures they get partially vacated. In that case, electrons can tunnel from the Co via these vacancy states into the graphite; effectively experiencing a reduced barrier height. It is plausible that the number of vacancies is quite high, because natural oxidation of deposited  $\text{Al}_2\text{O}_3$  is used instead of plasma oxidation of Al. Since no significant changes were made to the tunnel barrier fabrication process, defect-assisted tunneling probably occurred in all samples. Thickening the  $\text{Al}_2\text{O}_3$  layer for rotational deposition, the only modification, would only worsen the situation, since oxidation would be more difficult in a thicker layer.

However, there were some contacts that did show little temperature dependence with respect to their resistance. Though the value of their resistance was comparable to the ones in figure 4.2.8, they behaved largely Ohmic, with only small hints of non-linear behavior. This behavior could perhaps be attributed to pinholes. However, the resistance of these contacts was not dominated by tunneling, thus making the data unsuitable to draw conclusions with regard to the quality of the tunnel barrier.

### 4.3 MR and Hanle measurements

In order to measure the spin relaxation time a number of Hanle measurements were done over the course of thesis. However, these Hanle measurements gave only noise; no Hanle peak could be discerned from it. Explanations for this could be relatively high voltage noise, or because of a low Hanle signal due to low accumulation, which in turn would be caused by unreliable tunnel barriers. At that time it seemed wise to continue improving fabrication techniques, hopefully resulting in better tunnel barriers and thus a better shot at observing a Hanle peak.

The contacts used in figure 4.2.4 displayed good tunneling behavior and seemed reliable. These contacts were cooled to low temperatures in order to observe their performance in the low temperature range. However, at low temperatures only noise could be observed, which indicated that it had become an open circuit. Warming up again, these contacts did turn back on again around 230 K, but their electrical behavior had been changed irreversibly and they no longer displayed good tunneling behavior. The damage could be also seen visually in figure 3.4.11. As was discussed in chapter 3.4, it was then attempted to overcome this fabrication problem by changing the composition of the ferromagnetic stack, but this failed miserably. Due to recycling of older samples, no alternative, functioning samples were available anymore for a Hanle measurement. Since little time remained, and because the remaining graphite substrates were of mediocre quality, it was decided to quit fabrication and to invest the remainder of the time in an attempt to measure a Hanle signal.

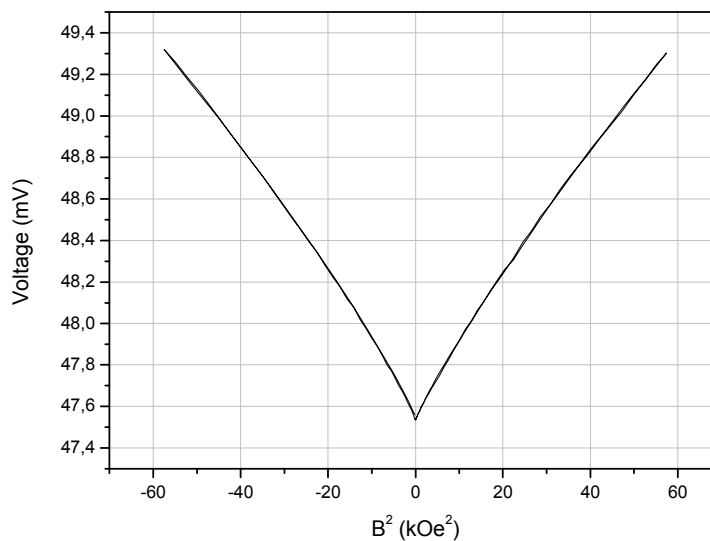


**Fig. 4.3.1:** Measurement of voltage between contact 4 and 4 (different devices), while sourcing a 2.5  $\mu$ A current between them, under a sweeping magnetic field at RT. The voltage is plotted as a function of the square of the magnetic field.

However, before the irreversible damage of the sample, an interesting measurement was done. Between two linear behaving contacts a current was sourced and the voltage was measured as a function of a perpendicular magnetic field; the result of which can be seen in figure 4.3.1. The behavior is similar to Lorentz magnetoresistance (LMR) and indeed conforms to some extent to equation 6. LMR is known to be very large in graphite, partly because of the long mean free path

lengths. The curve corresponds with other publications; having a quadratic dependence on B a low field and saturating in high fields [34].

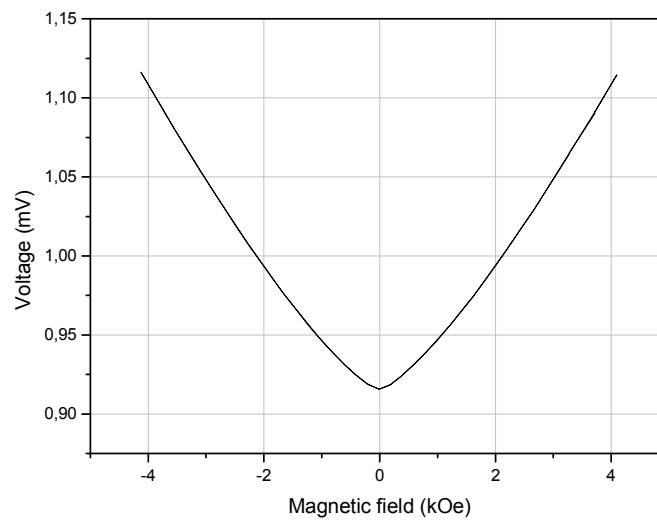


**Fig. 4.3.2:** Voltage measured between contacts 4 and 4 (different devices), while sourcing a  $93 \mu\text{A}$  current between 1 and 4 (same device) under a sweeping, perpendicular magnetic field at 5 K.

Luckily the big contacts (1 & 4) of the earlier discussed sample did not shut down at low temperatures. These contacts showed no non-linear behavior, which indicated that their tunnel barrier was unreliable. Ohmic contacts give low spin accumulation, which should result in a very low Hanle signal. However, even under these conditions a Hanle signal could, in principle, be measured, if the voltage noise is sufficiently low. Therefore, a lock-in amplifier was incorporated in the standard measurement equipment to boost sensitivity. As can be seen in figure 4.3.2, instead of a Hanle signal, a quasi LMR effect was observed in a three-terminal Hanle measurement. Even if a Hanle signal was present, its signature would have been swamped by the bigger LMR effect. The quasi-LMR effect was unexpected, since non-local probing schemes are supposed to suppress spurious effects from showing up. A possible cause could be that current paths extend throughout the material, so also extending (however small) underneath the external Hanle contact. Disturbance of the small current in this path by an external magnetic field could, in the case of graphite, be enough to give a sizable voltage response. Even a small quasi LMR effect could be enough to overwhelm a tiny Hanle effect in the case of Ohmic contacts.



## Chapter 5: Conclusions and recommendations

The goal of this project was to build electronic devices capable of measuring the spin relaxation time and length in thick (bulk) graphite, and to also subsequently measure these properties.

Despite the difficulty of working with graphite as a substrate, fabrication of these devices did seem possible. Vertical devices were made by shadow mask deposition and several methods were developed to fabricate lateral devices with different combinations of e-beam and photolithography. The vertical devices showed very low resistances ( $<100 \Omega$ ) and typical Ohmic behavior. Since Ohmic tunnel barriers were unlikely to result in a high spin accumulation, and because these devices were not suitable for non-local measurements, the fabrication of vertical devices was discontinued.

The fabrication of lateral devices by photolithography was ultimately more successful. However, fabrication results remained slightly unpredictable, because of the uniqueness of each individual sample due to its inherent (surface) features and variable properties after peeling/recycling. After a considerable investment of time, the fabrication problems in the areas of low resolution, lift-off and wire bonding, were more or less resolved.

However, the performance and reliability of the tunnel barriers remained problematic. Eventually, a new fabrication recipe seemed to have struck the right balance and to have yielded tunnel barriers with satisfactory properties. However, the contacts of these new devices were mechanically unstable during measurements in the low temperature regime; irreversibly damaging their electrical characteristics. A final fabrication run, with a ferromagnetic stack of a different composition to overcome this problem, did not yield any intact ferromagnetic contacts.

Due to the time spent in improvement of the fabrication methods, time-consuming wire bonding and high ratio of open-circuit contacts, only a limited amount of electrical measurement data was acquired. This data was not necessarily comparable to each other, since there were many fabrication modifications. Within the limited number of measurements, a large variance in behavior between measurements and between functioning contacts was observed. This was partly attributed to cracks in the contacts at the edges of the graphite channel. Tunneling behavior was only observed in two terminal measurements that included at least one small contact. This was attributed to the larger (defective) area of the big contacts; this also includes their far larger contact area at the steep edges of the graphite channel (figure 3.4.10b). No spin relaxation time and/or length could be determined; presumably due to the problematic tunnel barriers. A LMR curve was observed in a three terminal Hanle measurement and no Hanle signal could be extracted.

In conclusion, the two remaining obstacles to measuring the spin relaxation time and/or length seem to be the quality of the tunnel barriers and thermal stress between the ferromagnetic stack and graphite. It might be worthwhile for the latter to redo the fabrication run with the 100 nm thick cobalt. Though two such samples have been fabricated, this was carried out in a single run and some mistakes might have been made that caused an improper lift-off. Alternatively, stacks of  $\text{Al}_2\text{O}_3(1 \text{ nm})/\text{Co}(50 \text{ nm})/\text{Au}(3 \text{ nm})$  had been fabricated successfully beforehand. A stack of  $\text{Al}_2\text{O}_3(2 \text{ nm} - \text{rotated})/\text{Co}(50 \text{ nm})/\text{Al}(3 \text{ nm})$  should be equivalent. If the crack problem can be solved by depositing 25 nm Co and 25 nm Co under a  $180^\circ$  angle with respect to each other, potentially, a robust tunnel barrier could be fabricated.

An alternative could also be to invest time in reliably predicting the thickness of graphite flakes produced by exfoliation. The thickest flakes of this mesoscale graphite could be patterned with e-beam lithography, although this has already been done by several other groups [33], [35], [36].

## References

- [1] N. Tombros, C. Jozsa, M. Popinciuc, H.T. Jonkman, and B.J. van Wees, "Electronic spin transport and spin precession in single graphene layers at room temperature.," *Nature*, vol. 448, Aug. 2007, pp. 571-4.
- [2] J.F. Gregg, I. Petej, E. Jouguelet, and C. Dennis, "Spin electronics: a review," *Journal of Physics D: Applied Physics*, vol. 35, Sep. 2002, p. R121-R155.
- [3] V.A. Dediu, L.E. Hueso, I. Bergenti, and C. Taliani, "Spin routes in organic semiconductors.," *Nature materials*, vol. 8, Sep. 2009, pp. 707-16.
- [4] W.J.M. Naber, "Electron transport and spin phenomena in hybrid organic/inorganic systems," *PhD thesis*, 2010.
- [5] I. Zutic, J. Fabian, and S.D. Sarma, "Spintronics: Fundamentals and applications," *Reviews of Modern Physics*, vol. 76, 2004, pp. 323-410.
- [6] I.J. Marún-Vera, "Spin-Filter Scanning Tunneling Microscopy," *PhD thesis*, 2010.
- [7] J.S. Moodera, T.S. Santos, and T. Nagahama, "The phenomena of spin-filter tunnelling," *Journal of Physics: Condensed Matter*, vol. 19, Apr. 2007, p. 165202.
- [8] B.S. Sugahara and J. Nitta, "Spin-Transistor Electronics : An Overview and Outlook," *Proceedings of the IEEE*, vol. 98, 2010.
- [9] G. Schmidt, "Concepts for spin injection into semiconductors—a review," *Journal of Physics D: Applied Physics*, vol. 38, Apr. 2005, p. R107-R122.
- [10] S.P. Dash, S. Sharma, R.S. Patel, M.P. de Jong, and R. Jansen, "Electrical creation of spin polarization in silicon at room temperature.," *Nature*, vol. 462, Nov. 2009, pp. 491-4.
- [11] J. Takeya, M. Yamagishi, Y. Tominari, R. Hirahara, Y. Nakazawa, T. Nishikawa, T. Kawase, T. Shimoda, and S. Ogawa, "Very high-mobility organic single-crystal transistors with in-crystal conduction channels," *Applied Physics Letters*, vol. 90, 2007, p. 102120.
- [12] G. Szulczewski, S. Sanvito, and M. Coey, "A spin of their own.," *Nature materials*, vol. 8, Sep. 2009, pp. 693-5.
- [13] V. Karpan, G. Giovannetti, P. Khomyakov, M. Talanana, a Starikov, M. Zwierzycki, J. van den Brink, G. Brocks, and P. Kelly, "Graphite and Graphene as Perfect Spin Filters," *Physical Review Letters*, vol. 99, Oct. 2007.
- [14] V.M. Karpan, P. a Khomyakov, a a Starikov, G. Giovannetti, M. Zwierzycki, M. Talanana, G. Brocks, J. van den Brink, and P.J. Kelly, "Theoretical prediction of perfect spin filtering at interfaces between close-packed surfaces of Ni or Co and graphite or graphene," *Physical Review B*, vol. 78, Nov. 2008, pp. 1-11.
- [15] J. Maassen, W. Ji, and H. Guo, "Graphene spintronics: the role of ferromagnetic electrodes.," *Nano letters*, vol. 11, Jan. 2011, pp. 151-5.
- [16] J. Velev, P. Dowben, E. Tsymbal, S. Jenkins, and a Caruso, "Interface effects in spin-polarized metal/insulator layered structures," *Surface Science Reports*, vol. 63, Sep. 2008, pp. 400-425.
- [17] M. Baumer, J. Libuda, and H.J. Freund, "The temperature dependent growth mode of nickel on the basal plane of graphite," *Surface science*, vol. 327, 1995, p. 321–329.

- [18] S.W. Poon, J.S. Pan, and E.S. Tok, "Nucleation and growth of cobalt nanostructures on highly oriented pyrolytic graphite," *Physical chemistry chemical physics : PCCP*, vol. 8, Jul. 2006, pp. 3326-34.
- [19] N. Tombros, S. Tanabe, a Veligura, C. Jozsa, M. Popinciuc, H. Jonkman, and B. van Wees, "Anisotropic Spin Relaxation in Graphene," *Physical Review Letters*, vol. 101, Jul. 2008, pp. 2-5.
- [20] L.E. Hueso, J.M. Pruneda, V. Ferrari, G. Burnell, J.P. Valdés-Herrera, B.D. Simons, P.B. Littlewood, E. Artacho, A. Fert, and N.D. Mathur, "Transformation of spin information into large electrical signals using carbon nanotubes.," *Nature*, vol. 445, Jan. 2007, pp. 410-3.
- [21] K.S. Novoselov, a K. Geim, S.V. Morozov, D. Jiang, Y. Zhang, S.V. Dubonos, I.V. Grigorieva, and a a Firsov, "Electric field effect in atomically thin carbon films.," *Science (New York, N.Y.)*, vol. 306, Oct. 2004, pp. 666-9.
- [22] Z.-yu Juang, Y.-liang Zhong, F.-rong Chen, and L.-jong Li, "Direct Formation of Wafer Scale Graphene Thin Layers on Insulating Substrates by Chemical Vapor Deposition," *Nanoletters*, 2011, pp. 1-5.
- [23] V.Y. Aristov, G. Urbanik, K. Kummer, D.V. Vyalikh, O.V. Molodtsova, A.B. Preobrajenski, A. a Zakharov, C. Hess, T. Hänke, B. Büchner, I. Vobornik, J. Fujii, G. Panaccione, Y. a Ossipyan, and M. Knupfer, "Graphene synthesis on cubic SiC/Si wafers. perspectives for mass production of graphene-based electronic devices.," *Nano letters*, vol. 10, Mar. 2010, pp. 992-5.
- [24] S. Thalabard, "A study of the Hanle effect in spin devices with ohmic contacts," *Internship report*, 2008, pp. 1-32.
- [25] F.J. Jedema, H.B. Heersche, A.T. Filip, J.J.A. Baselmans, and B.J. van Wees, "Electrical detection of spin precession in a metallic mesoscopic spin valve," *Nature*, vol. 416, 2002, pp. 713-716.
- [26] SPI supplies, *SPI-2 grade HOPG*.
- [27] J. Winterlin and M.-L. Bocquet, "Graphene on metal surfaces," *Surface Science*, vol. 603, Jun. 2009, pp. 1841-1852.
- [28] MichroChemicals GmbH, *TI-35ES*.
- [29] J. Lemmens, "Rubrene single-crystal FETs with ferromagnetic contacts," *Master thesis*, 2008.
- [30] MicroChemicals GmbH, "Processing image reversal resists," *Product description manual*, 2003.
- [31] The engineering toolbox, "Coefficients of linear expansion.," *Engineering website*, [http://www.engineeringtoolbox.com/linear-expansion-coefficients-d\\_95.html](http://www.engineeringtoolbox.com/linear-expansion-coefficients-d_95.html), accessed on 12-9-2011
- [32] SPI supplies, *SPI fast setting conductive silver epoxy*.
- [33] J. Barzola-Quiquia and P. Esquinazi, "Spin transport in a thin graphite flake," *Journal of Materials Science*, vol. 46, Feb. 2011, pp. 4614-4617.
- [34] H. Pal and D. Maslov, "Necessary and sufficient condition for longitudinal magnetoresistance," *Physical Review B*, vol. 81, Jun. 2010, pp. 1-6.
- [35] W.H. Wang, K. Pi, Y. Li, Y.F. Chiang, P. Wei, J. Shi, and R.K. Kawakami, "Magnetotransport properties of mesoscopic graphite spin valves," *Physical Review B*, vol. 77, Jan. 2008, pp. 1-4.
- [36] M. Nishioka and a M. Goldman, "Spin transport through multilayer graphene," *Applied Physics Letters*, vol. 90, 2007, p. 252505.

## Appendix A: Procedures and recipes

### DCA procedures

Many people in the NE-group know how to work with the DCA deposition equipment and the overall procedures. In this section I will not explain the overall procedures that are used in the DCA, but would like to point out some that were crucial and unique to my project.

First of all, usually position 9 of the sample holder (see figure A.1) at 90° is used to deposit materials; all the tooling factors are also calibrated with respect to this position. However in conjunction with lift-off this position causes problems. Material is piled onto one side of the side-wall, making the lift-off difficult. So instead of using position 9, we use position 12, 11 or 6 at 90°. However tooling factors for these positions are different than those for position 9; differences up to 20% have been observed. I used to have a calibration for this, but since because the DCA has been opened and the crystal growth monitors have been changed these values have likely become outdated and so a new calibration would be needed.

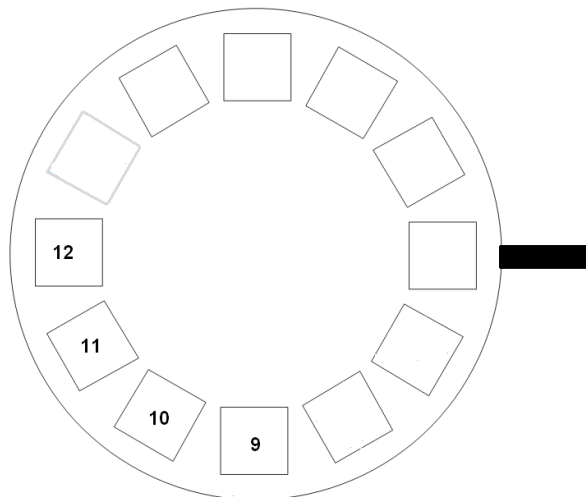


**Fig. A.1:** Positions on the shadow mask relative to the stem of the holder. Only the numbering of positions 9-12 is displayed, but the rest of the positions are numbered in the same clock-wise fashion.

Apart from the positions on the sample holder, creating a tunnel barrier was also a bit different for my process. Plasma oxidation would probably have affected the carbon-atoms in the graphite and so  $\text{Al}_2\text{O}_3$  was directly deposited on the substrate. To ensure large area coverage of the sample,  $\text{Al}_2\text{O}_3$  is deposited consecutively from four different angles. Special care should be taken with heating up the tunnel barrier material, since fast melting can affect the rate and the quality. After depositing the  $\text{Al}_2\text{O}_3$  deposition samples are put into the load lock of the DCA for half an hour in a pressure of at least 100 mTorr of pure oxygen.

## Graphite substrate preparation

- Cut a substrate
  - Use a knife to cut/grind along graphite sample along a ruler.
  - Cut the upstanding ridges, without touching the regular surface.
- Peel the surface with Scotch tape
  - Wind the back of Scotch tape of a very thin rod.
  - Use the tip of this rod to pick/roll the edges of the substrate to remove the remains of the ridges.
  - Try to remove loose patches at the surface with the rod.
  - Roll the surface gently with a rod trying in several directions, trying to remove one layer in one roll. The diagonal direction is usually the most successful as last roll.
  - Inspect with magnifying glass.
  - Cut a tiny mark in the backside of graphite substrate to make orientation identification later possible. Make sure this mark is nowhere near the middle, since this would hamper suction used in photoresist spinning.
- Put the finished substrate in ultrasonication bath of acetone at power level 7 for 10 minutes in order to remove loose patches, thus further ensuring structural integrity during later steps and to remove traces of remains of earlier applied photoresist.

## Photolithography

- Measure thickness of the substrate.
  - The difference in required thickness should be compensated in the photolithography sample holder with several layers of tape. Each layer is equivalent with 60-80  $\mu\text{m}$ .
- Put the substrate in ultrasonication bath of ethanol at power level 7 for 10 minutes in order to clean the surface and to remove the rests of acetone.
  - Blow the sample mildly dry with nitrogen. Make sure it is really dry.
- Apply the photoresist TI-35ES.
  - Use the smallest spinhead with a sharp conical tip.
  - Balance the graphite substrate exactly in the middle; the rough surface of graphite does not give optimal suction. Failure to balance it might lead to loss and destruction of samples.
  - Spin the photoresist at 4000 rpm for 20 seconds.
  - Soft bake at 95 °C for 2 minutes.
- Place the sample in the photolithography sample holder.
  - Make sure that with every sample the correct layer thickness is used.
- First exposure.
  - Insert the right parameters for approach. For each sample a safe approach distance should be used, depending on the insecurities about their combined thickness (with tape layers) and the presence of ridges.
  - Expose for 24 second.
- Wait for 30 minutes.
  - Covering the samples is desired.
- Post exposure bake for 2 minutes at 120 °C.
- Flood exposure for 1 minute
  - Approach distances are not that relevant anymore.

- Development in OPD4262.
  - Develop for 60 seconds (critical), while moving the sample(s).
  - Put the sample directly afterwards straight into a beaker of DI-water for 15 seconds, while moving.
  - Shower the sample afterwards for 45 seconds gently. Try not target the spray directly unto the present pattern.
  - Spin-dry at moderate-low speeds for 60 seconds.

### Lift-off

- Leave the sample in acetone overnight (at least 3 hours).
- Afterwards put the sample in ultrasonic bath of acetone for 5 seconds at power level 5.
  - Should sometimes be done twice for SiO<sub>2</sub> layers.
  - Remove remaining material from vital spots (if necessary) by spraying acetone from for example a squeeze. Try to always spray along the direction of the ferromagnetic contacts. Usually the material should come off relatively quickly, but a tiny patch will usually remain.
- Soak the sample in IPA for 10 minutes.
  - Blow mildly dry with nitrogen. Make sure it's really dry.

### E-beam resist PMMA

- Put the substrate in ultrasonication bath of ethanol at power level 7 for 10 minutes in order to clean the surface and to remove the rests of acetone.
  - Blow the sample mildly dry with nitrogen. Make sure it is really dry.
- Apply the photoresist PMMA.
  - Spin the photoresist at 1500 rpm for 20 seconds.
  - Soft bake at 150 °C for 2 minutes.
- Exposure with e-beam at 15 kV and with a dose of 99.975 μC/cm<sup>2</sup>.
- Development in MIBK.
  - Develop for 60 seconds (critical), while moving the sample(s).
  - Put the sample directly afterwards straight into a beaker of IPA for 15 seconds, while moving.
  - Blow mildly dry with nitrogen. Make sure it's really dry.

### Lift-off:

Lifting off a deposited layer with an e-beam pattern has been previously attempted once in a similar manner as the recipe in the previous paragraph. However the pattern started to break, before enough material could be removed.

This attempt however did not use any of the lift-off deposition positions described above. It might be that if that would have been the case, the lift off would have succeeded. Even if that would be the case there would be still the problem with the contacts. The-beam photoresist cannot be any thicker than 100 nm, which also results in contacts thinner than 100 nm. Due to the unevenness of the HOPG samples, such thin contacts tend to be rather fragile. The conclusion could be that even if we got the lift-off to work, during the electrical measurements the fragility of the contacts might surface, making the contact useless. That is why we discontinued this branch and why it is not resolved whether the lift-off is possible or not.

## Shadow mask deposition

- Use a graphite substrate that has previously been prepared.
- Place the graphite substrate in the sample holder.
- Move the deposition holder into the main chamber of the DCA.
  - Deposit a 1 nm layer of  $\text{Al}_2\text{O}_3$ .
  - Return the sample holder to the loadlock. Fill the loadlock with  $\text{O}_2$  up to a pressure of 100 mTorr and let the  $\text{Al}_2\text{O}_3$  oxidize for 30 minutes.
  - Return the sample holder to the main chamber and deposit an additional 50 nm of Co and 3 nm of Au as a capping layer.
  - Remove the sample holder from the DCA.
- The next step is to separate the deposited layers and the upper graphite layers from the bulk substrate.
  - Put double sided, conducting tape on top of a solid object with preferably a top surface of a similar size as the substrate.
  - Put the top side of the substrate on the bare surface of the tape and make sure it is firmly attached.
  - Separate the bulk substrate very evenly from the tape using tweezers (tricky).
  - Remove the double sided tape gently from the solid object.
  - Attach double sided tape to a dummy Si substrate, leaving the deposited side bare.
- Place the hybrid substrate in the sample holder.
  - Add the shadow mask on the substrate and the sample holder.
- Move the sample holder into the main chamber of the DCA.
  - Use the triggering mechanism to rotate the shadow mask, until the substrate is underneath one of the “open” positions of the shadow mask.
  - Deposit a 1 nm layer of  $\text{Al}_2\text{O}_3$  everywhere.
  - Return the sample holder to the loadlock. Fill the loadlock with  $\text{O}_2$  up to a pressure of 100 mTorr and let the  $\text{Al}_2\text{O}_3$  oxidize for 30 minutes.
  - Return the sample holder to the main chamber. Use the triggering mechanism again to rotate the shadow mask to the “pattern” position.
  - Deposit 50 nm of permalloy and 3 nm of Al as a capping layer.
  - Remove the sample holder from the DCA.

## Appendix B: Mask designs

This section shows some mask designs used in this thesis. This appendix has different subsection for masks used in photolithography, e-beam lithography and shadow mask deposition.

### Photolithography masks

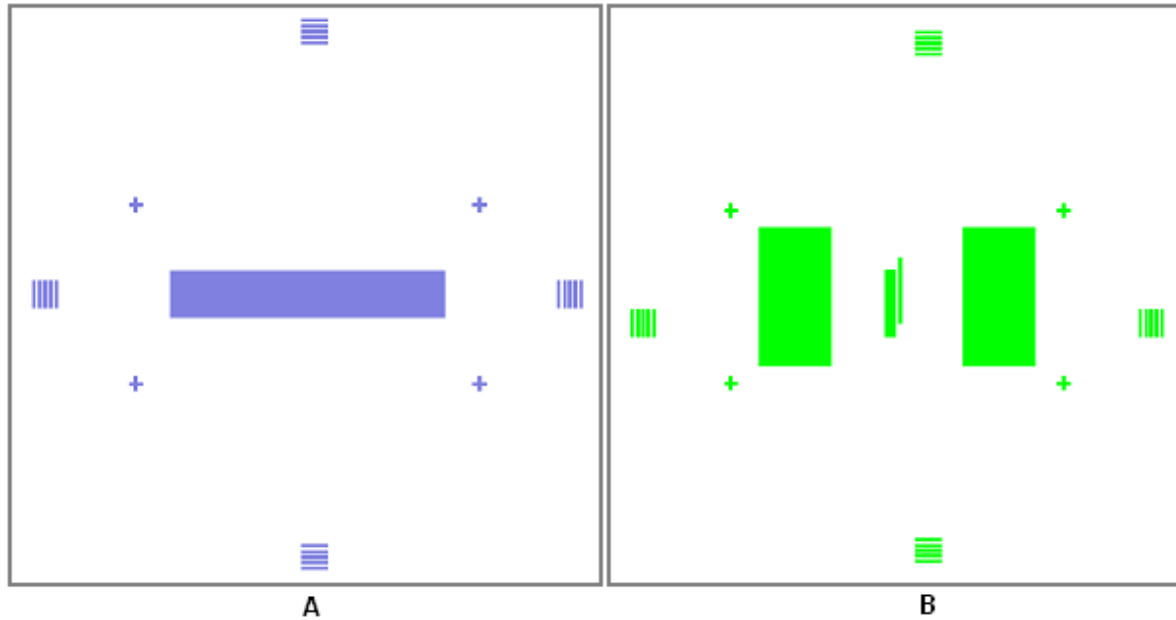
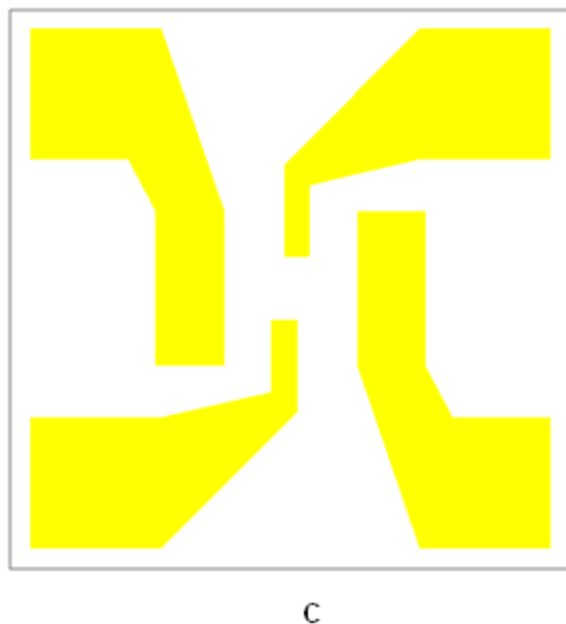


**Fig. B.1:** Close up of a single device on the three different photo masks. Each photo mask contained 7x5 devices. **(a)** Inverse mask for defining the channel in the SiO<sub>2</sub>. The length of the channel was 400  $\mu\text{m}$  and its width varied (20, 32, 44, 56 and 68  $\mu\text{m}$ ). **(b)** Mask for defining the ferromagnetic contacts. The two smaller contacts have both a length 100  $\mu\text{m}$ , while having widths of 4 and 16  $\mu\text{m}$ , respectively. Their separation distance varied (2.0, 2.5, 3.0, 3.5, 4.0, 4.5 and 5.0  $\mu\text{m}$ ). **(c)** Mask for defining the contact pads. Picture size is approximately 800 x 800  $\mu\text{m}$ .



## E-beam lithography masks

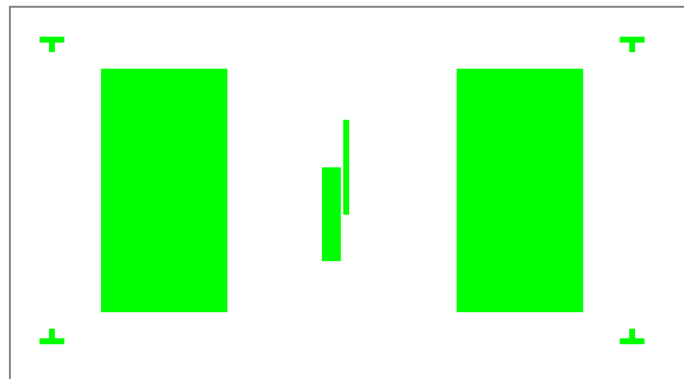


**Fig. B.2:** Close up of a single device in the file used for the e-beam writing. Note the slight vertical translation of the small contacts with respect to each other; a modification of the original photo mask to combat the stitching problems. A row of 7 different devices would be done in a single writing run; with the separation distance between the smaller contacts varying (3x 2.0, 2x 1.5 and 3x 1.0  $\mu\text{m}$ ).

## Shadow mask deposition masks

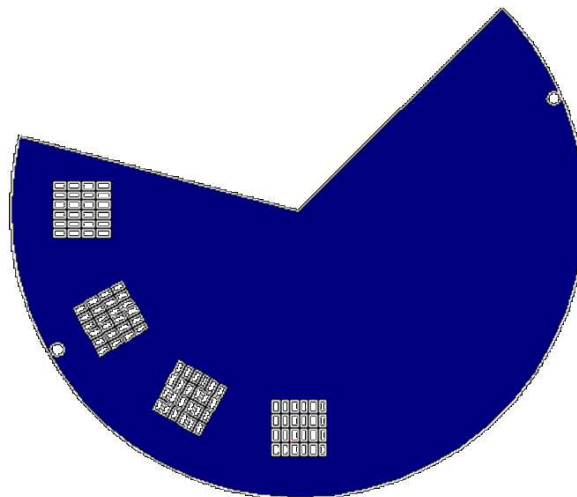


**Fig. B.3:** Shadow mask used during deposition of the vertical devices. The mask is divided into 12 positions (equally divided between the positions “open”, “closed” and “pattern”) to allow for the patterning of 4 substrates in a single deposition run. The pattern consists out of 24 contacts of 2.3 x 1.5 mm, with small separations in between the contacts.